DEVELOPING A SEMI-ANALYTICAL MODEL FOR ROTOR WHIRL PREDICTION

A Thesis submitted in partial fulfillment of the requirements for the award of the Degree of

BACHELOR OF TECHNOLOGY

BY

RIJU CHATTERJEE

(BTECH/10015/18)
MECHANICAL ENGINEERING

UNDER THE GUIDANCE OF
**DR. NIRMAL KUMAR, ASSISTANT PROFESSOR.**
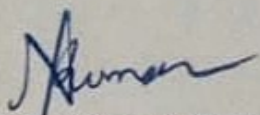
DEPARTMENT OF MECHANICAL ENGINEERING
BIRLA INSTITUTE OF TECHNOLOGY
MESRA - 835215, RANCHI
2022

DECLARATION CERTIFICATE

This is to certify that the work presented in the thesis entitled "Developing a Semi-Analytical Model for Rotor Whirl Prediction" in partial fulfillment of the requirement for the award of the Degree of BACHELOR OF TECHNOLOGY in Mechanical Engineering at Birla Institute of Technology Mesra, Ranchi is an authentic work carried out under my/our supervision and guidance.

To the best of my knowledge, the content of this thesis does not form a basis for the award of any previous Degree to anyone else.

Dr. Nirmal Kumar
Dept. of Mechanical Engineering
Birla Institute of Technology
Mesra, Ranchi
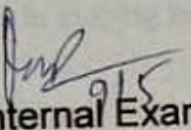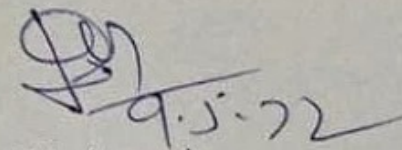
CERTIFICATE OF APPROVAL

The following thesis entitled "**Developing a Semi-Analytical Model for Rotor Whirl Prediction**", is hereby approved as a creditable study of rotor dynamics and has been presented in satisfactory manner to warrant its acceptance as prerequisite to the degree "Bachelor of Technology" in Mechanical Engineering.

It is understood that by this approval, the undersigned do not necessarily endorse any conclusion drawn or opinion expressed therein, but approve the thesis for the purpose for which it is submitted.

(Internal Examiner)   (External Examiner) 9/5/22

(Chairman)

Head of Department

Mechanical Engineering

Birla Institute of Technology, Mesra

2

Acknowledgement
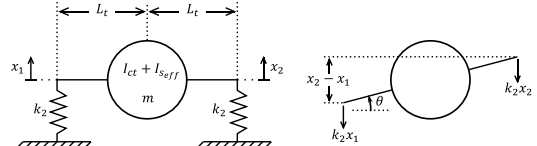
Abstract

Most fully analytical treatments of rotor whirl are restricted to very simple rotor geometries, and have limited use while studying real-world rotors. Analysis of more complex rotors is routinely carried out in Finite Element software such as Ansys, but this is less effective at generating fundamental insights to inform the design process. This thesis presents the development of a rotor model of intermediate complexity. Fully analytical Newtonian approaches to estimating rotor whirl are first demonstrated via examples. The new semi-analytical model is then introduced, wherein the rotor's rigidity and inertia are considered to vary along its length as functions of spatial coordinate x. Predictions of whirl speeds are obtained through a Lagrangian formulation with assumed modes. This method can accommodate axisymmetric rotors with variation in cross-section or material properties, or both. The method is first demonstrated on simple and analytically tractable rotor geometries. Next, it is applied to a real sCO_2 rotor design, for which the rotor properties' x-dependence is approximated by curves fit to a small number of datapoints obtained from simpler (non-rotordynamic) simulations. All analytical results are validated against results from rotordynamic simulations performed in state-of-the-art FEM software.
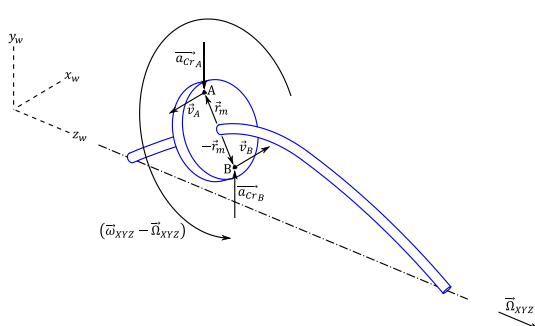
Graphical Abstract
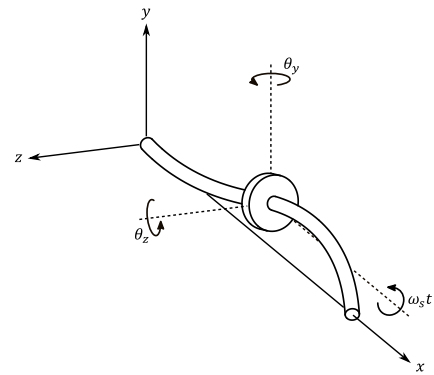
The simplest spring-mass rotor whirl treatment
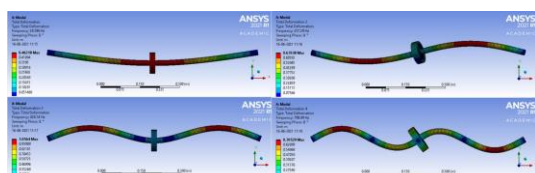
Discrete analogy to second bending mode
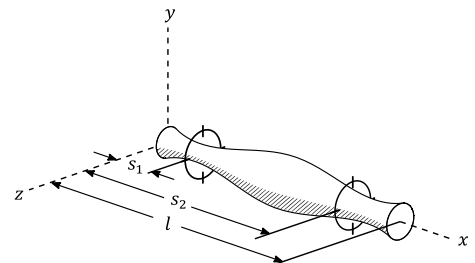
The Coriolis effect in a whirl-synchronized reference frame
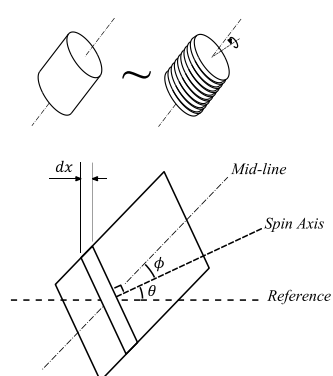
Orientation angles in a thin-disc rotor model
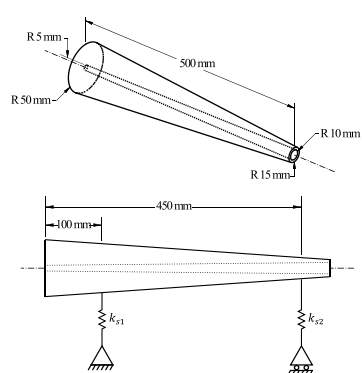
Whirl modes found in Ansys for validation
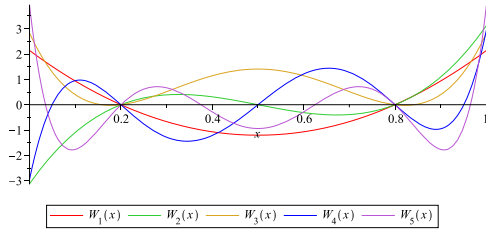
A general axisymmetric rotor
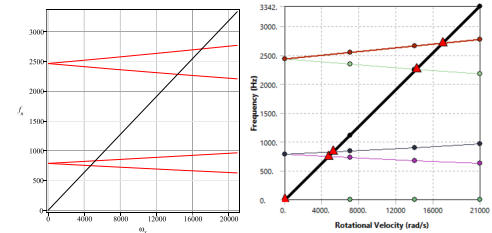
Shear angle in a Timoshenko rotor
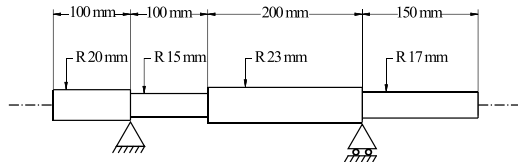
A tapered hollow rotor
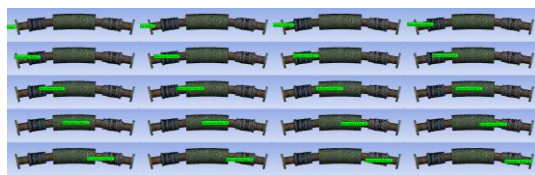
Orthogonalized polynomial assumed mode basis with forced roots
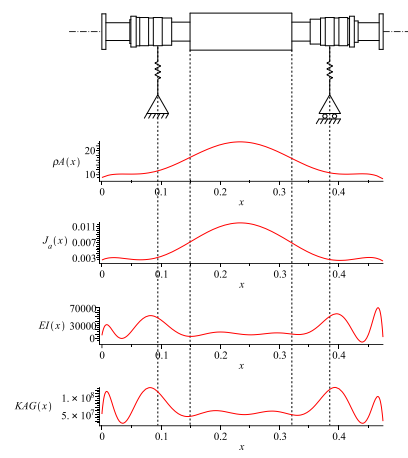
Campbell diagrams from analytical formulation and Ansys
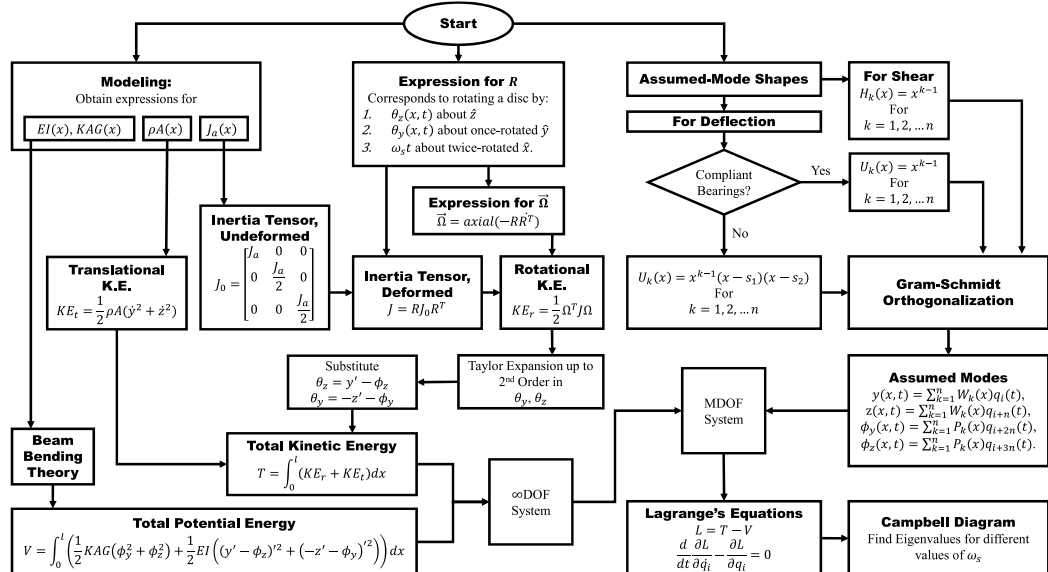
A multi-stepped rotor

Finding datapoints for rotor stiffness from static structural simulation

Polynomial-fit rotor model

Semi-analytical whirl prediction method overview

Table of Contents

1. INTRODUCTION

Whirl occurs when the spin speed of a rotor matches its natural frequency of lateral vibration, causing a resonance condition where excitation due to inertial forces from small mass eccentricities leads to large vibration responses. The speeds at which this happens are called critical speeds and form one of the most important mechanical characteristics of a rotor system from an operational point of view.

The whirling motion can effectively be seen as simultaneous bending vibration in two planes, superimposed on the spinning of the rotor. For many rotors, therefore, the critical speeds are very close to and can be meaningfully approximated by the natural frequencies of bending vibration. This approximation, however, typically becomes increasingly inaccurate for higher modes – and particularly so in the case of asymmetric mass/inertia distribution about the middle of the shaft – due to the effect on natural frequencies of so-called gyroscopic or Coriolis effects, which cause each bending mode to diverge, as the speed of the rotor increases, into two branches: one each for forward and backward whirl [1].

One of the main reasons that sCO_2 is attractive as a thermodynamic medium is that its high density allows for power generation units that are far more compact than steam or gas-operated systems of similar capacity. However, this necessitates much higher turbine speeds in sCO_2 systems than are common with traditional systems. Whereas a low-speed rotor may be designed to be run exclusively below its first critical speed, a high-speed rotor such as an sCO_2 turbine is commonly operated above one or more critical speeds [2]. As such, it is particularly important with sCO_2 rotors to understand the higher whirl modes, and rotordynamic analyses capable of finding more than one whirling mode are required.

Since gyroscopic precession is inherently a three-dimensional phenomenon, rotordynamic analyses that aim to capture gyroscopic effects must necessarily deal with complex three-dimensional motions involving combinations of rotations and translations. As such, Lagrangian formulations are often preferred since they yield more elegant and tractable expressions in these situations than their Newtonian counterparts might. Additionally, given the paramount importance to gyroscopic terms of the orientation of spinning elements along the shaft, Timoshenko-like beam theories (in which plane sections are considered to remain plane but not necessarily normal to the

beam mid-line) have proved very successful. Choi et al. [3] derived equations of motion for a Timoshenko rotor using three different formulations and showed that while traditionally, rotor equations have been written in Lagrangian formulations by introducing gyroscopic effects through generalized work terms, they in fact emerge organically given a consistent reference frame. Han and Zu [4] derived the equations of motion for a spinning Timoshenko beam subject to a moving load analytically in closed form.

While uniform rotors allow for elegant analytical models, treatments of more complex rotors are often of greater practical use, and are more relevant to this work. Laura et al. [5] presented a method to use polynomial assumed modes to calculate whirl speeds for stepped shafts with multiple intermediate supports; gyroscopic and shear effects were not considered. Shiau and Hwang [6] presented an assumed modes approach to the dynamic characteristic of undamped rotor-bearing systems consisting of discs mounted on uniform and internally stepped shafts. Fang and Yang [7] modelled complex rotor systems using Distributed Transfer Function Synthesis; gyroscopic terms were added separately. Norouzi et al. [8] presented a method to use assumed modes to derive equations for a rotor with multiple disks, bearings, and mass unbalances. Afshari and Rahaghi [9] demonstrated the use of a Newtonian formulation and the Differential Quadrature Method to analyze stepped rotors with multiple bearings.

Analyses involving rotors whose physical characteristics vary along their axis are of particular relevance here. Mahadevan et al. [10] demonstrated the use of modal projections to obtain whirl speeds of arbitrary axisymmetric rotors through a three-dimensional continuum treatment of rotor geometry and an inertial prestress-based accounting of gyroscopic effects; only forward synchronous whirl was studied. Whalley and Abdul-Ameer [11] developed a model for the whirling of shafts of varying diameter using transfer functions. Work on rotors constructed from Functionally Graded Materials bears relevance to treatments of rotors with axially variable material properties, although such effects in FGMs are more local, generally assumed to vary as a power law. Huang et al. [12] investigated the effects of an axially functionally graded material on rotor whirl speeds. Elhannani et al. [13] analyzed a functionally graded tapered rotor shaft system.

The sCO$_2$ rotor of interest to this thesis has a laminated core for electrical generator windings. The mechanical properties assumed here for the laminated core are based on work by Garvey [14], who characterized the vibrational behaviour of electrical laminates, and by Garvey et al. [15], who applied these findings to rotor systems and described typical effective material properties of laminated cores in rotors.

Since the natural frequencies of lateral vibration of a rotor can often serve as very useful first approximations to its whirl speeds, this thesis begins by demonstrating how well-known results from vibration theory can be used to calculate lateral vibration frequencies for simple rotor examples. Next, Coriolis or gyroscopic effects, which cause whirl frequencies to diverge from lateral vibration frequencies, are described. A fully analytical Newtonian formulation with transcendental equations is then presented for a rotor consisting of a rigid disc on a thin shaft. The semi-analytical model is then presented, wherein a Lagrangian formulation is illustrated for axisymmetric rotors where linear mass density ρA, effective flexural rigidity EI, effective shear rigidity KAG, and the axial mass moment of inertia per unit length J_a, are taken to vary as functions of spatial coordinate x along the nominal rotor axis. Orthogonalized polynomial bases of assumed modes are used for the deflection and shear in the rotor. Explorations of such a combination of a multi-parameter one-dimensional rotor model with an assumed modes formulation are not easily found in previous literature. Also, unlike most previous assumed modes treatments of rotor whirl, the model developed here does not use ad-hoc inertial forces to account for gyroscopic effects, allowing them instead to emerge organically by writing all energy expressions from the static reference frame. The approach is first demonstrated on simple rotor geometries both on rigid and on compliant bearings, and results are compared with industry-standard Finite Element software Ansys. The method is then applied to a more complex real-world rotor example, for which $\rho A(x)$, $EI(x)$, $KAG(x)$, and $J_a(x)$ are approximated by curves fit to a small number of datapoints obtained from simpler (non-rotordynamic) simulations.

2. ROTOR VIBRATION EXAMPLES WITHOUT SPIN

Rotor whirl can accurately be described as bending vibration combined with spinning. As the spin speed increases, gyroscopic or Coriolis effects cause the natural frequencies to change, thus causing the critical speeds or the whirl speeds to diverge from bending vibration frequencies observed when the rotor is not spinning. For a very large class of realistic rotors, however, the extent of this departure is relatively small. The lateral vibration frequencies of the stationary rotor are therefore perfectly adequate estimates of the whirl speed. This section demonstrates critical speed estimation through calculation of natural frequencies of lateral vibration, using well-known standard results from vibration theory.

2.1. Estimating Three Critical Speeds for a Simple Rotor

The goal is to calculate critical speeds of a simply-supported steel rotor that consists of a shaft of length L and diameter d, and a concentric cylinder of length $\frac{L}{8}$ and diameter $D = 4d$ mounted midway. The results are to be verified using Finite Element Analysis in Ansys.
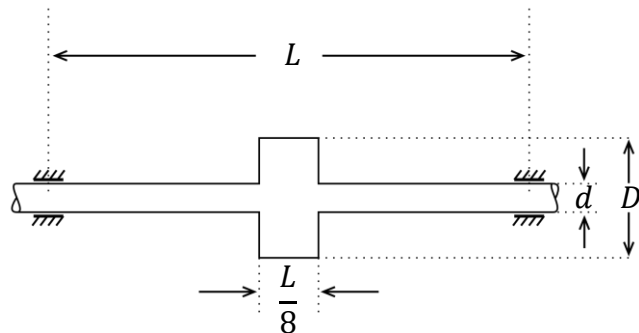
Figure 1: Proportions of the rotor

2.1.1. Whirling of The Rotor at 1st Critical Speed

During whirling, the rotor shaft experiences a lateral deflection due to the centrifugal effect.

12
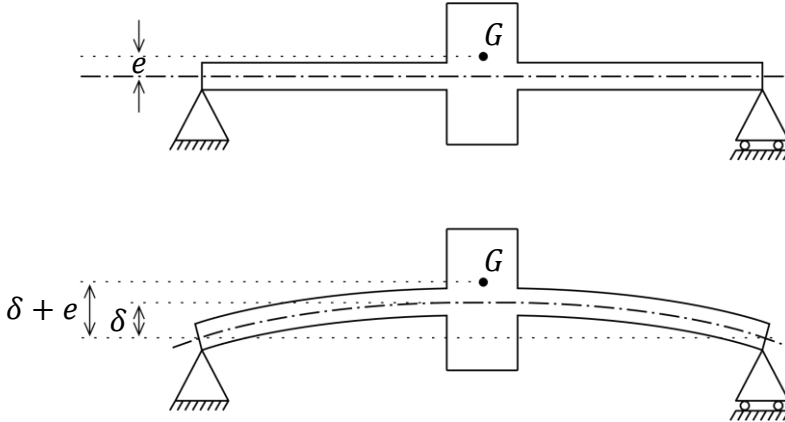
Figure 2: Rotor in undeflected and deflected state

In the undeflected state, the center of mass G of the rotor is offset from the axis of rotation by an eccentricity e. Since the rotor in question is nominally axisymmetric, e approaches zero as manufacturing tolerances improve. During whirling, the middle of the rotor experiences a lateral deflection δ.

Assuming that the center of mass remains in line with the direction of the deflection, the effective radius of gyration in the deflected state is $\delta + e$.

The two supports provide reaction forces R_A and R_B.
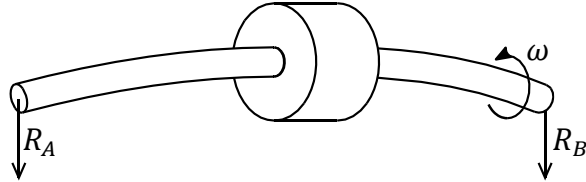
Figure 3: Free-body diagram of whirling rotor

Due to the symmetry of the system, the reactions R_A and R_B at the two supports are equal, and their combined effect is that of a net force in response to and in the opposite direction as the deflection.

The rotor can thus be thought of as a spring-mass system with a spring constant k equal to the effective lateral stiffness of the shaft at its mid-point:
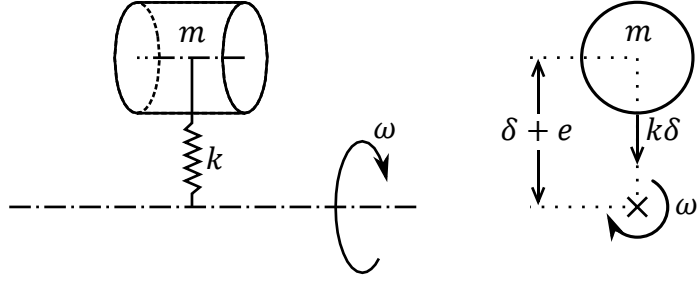
Figure 4: Spring-mass picture of whirling rotor

The center of mass of the rotor is experiencing centripetal acceleration $\omega^2(\delta + e)$ caused by the restoring force $k\delta$.

$$k\delta = m\omega^2(\delta + e)$$

$$k\delta = m\omega^2\delta + m\omega^2 e$$

$$k\delta - m\omega^2\delta = m\omega^2 e$$

$$\delta = \frac{m\omega^2 e}{k - m\omega^2}$$

$$\delta = \frac{\omega^2 e}{\dfrac{k}{m} - \omega^2} \tag{1}$$

As ω approaches $\sqrt{\dfrac{k}{m}}$, the denominator on the RHS of eq. (1) goes to zero, so δ becomes large. $\sqrt{\dfrac{k}{m}} = \omega_n$ gives the critical speed of the shaft.

2.1.1.1. Massless Shaft Approximation

A first approximation can be arrived at by ignoring the mass of the shaft and approximating the cylinder with a point mass. This mass, m_c, is given by the density of steel times the volume of the cylinder:

$$m_c = \rho \times \frac{\pi D^2}{4} \times \frac{L}{8} = \frac{\rho\pi(4d)^2 L}{32} = \frac{\rho\pi d^2 L}{2} \tag{2}$$

The stiffness of the shaft can be calculated using the expression for deflection of a simply supported beam loaded in the middle.
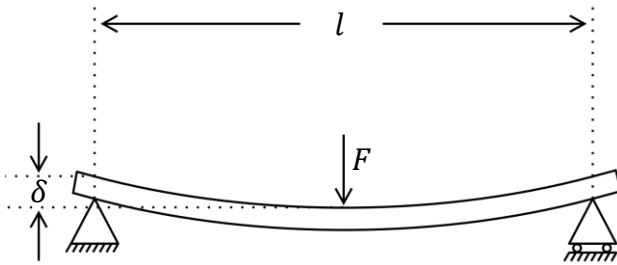
Figure 5: Deflection of a simply supported beam

The deflection is given by:

$$\delta = \frac{Fl^3}{48EI}$$

Where E is Young's Modulus for the beam and I is the area moment of inertia of the beam's cross-section.

Here, l can be taken to be $\frac{7}{8}L$ since the central cylinder prevents $\frac{1}{8}$ of the shaft from bending significantly. Now the stiffness can be expressed as:

$$k = \frac{F}{\delta} = \frac{48EI}{l^3} = \frac{24576EI}{343L^3} \tag{3}$$

For the circular shaft, the area moment of inertia of the cross-section is:

$$I = \frac{\pi d^4}{64} \tag{4}$$

Substituting the expression from (4) into (3),

$$k = \frac{24576E}{343L^3} \times \frac{\pi d^4}{64} = \frac{384E\pi d^4}{343L^3} \tag{5}$$

From the stiffness and mass of the cylinder, the natural frequency can be calculated as:

$$\omega_n = \sqrt{\frac{k}{m_c}} = \sqrt{\frac{\frac{384\pi E d^4}{343L^3}}{\frac{\rho\pi d^2 L}{2}}} = \sqrt{\frac{768E d^2}{343\rho L^4}} \tag{6}$$

15

2.1.1.2. Correction Term for Mass of Shaft

If gyroscopic effects are ignored, the whirling motion can be seen as a superposition of planar vibration in two directions, 90 degrees out of phase.

So far, the mass of the shaft itself has been ignored. The error caused by this can be partially corrected for by modelling the effect of the mass of the shaft as an additional effective mass at the mid-point.

The total mass of the shaft is given by its density times its volume:

$$m_s = \rho \times \frac{\pi d^2}{4} \times \frac{7}{8} L = \frac{7 \rho \pi d^2 L}{32} \tag{7}$$

Now, the deflected profile of the shaft is approximated by a sinusoid of amplitude A:
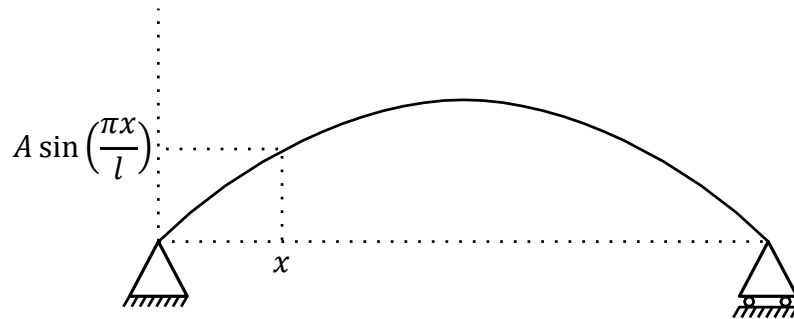
Figure 6: Assumed deflection profile of shaft

Deflections are small, so the mass of the shaft is distributed evenly over l with linear mass density $\frac{m_s}{l}$.

The velocity of a point on the beam at position x and time t (for planar vibration of the shaft) is given by:

$$v(x,t) = \frac{\partial}{\partial t}\left[A \sin\left(\frac{\pi x}{l}\right)\right] = \dot{A} \sin\left(\frac{\pi x}{l}\right)$$

So, the kinetic energy at point x is:

$$KE_x = \frac{1}{2} \times \frac{m_s}{l} dx \times \left[\dot{A} sin\left(\frac{\pi x}{l}\right)\right]^2$$

and the total kinetic energy is:

$$KE = \frac{m_s \dot{A}^2}{2l} \int_0^l \left[sin\left(\frac{\pi x}{l}\right) \right]^2 dx = \frac{m_s \dot{A}^2}{2l} \left(\frac{l}{2}\right) = \frac{m_s \dot{A}^2}{4} \tag{8}$$

The velocity at the mid-point of the shaft is $\dot{A}$. If the distributed mass of the shaft were replaced with an effective mass $m_{s_{eff}}$ at the mid-point, the kinetic energy would be:

$$KE = \frac{1}{2} \times m_{s_{eff}} \times \dot{A}^2 = \frac{\dot{m}_{s_{eff}} \dot{A}^2}{2} \tag{9}$$

Equating the kinetic energy due to the distributed mass (8) with the kinetic energy due to the concentrated effective mass (9) gives:

$$\frac{m_s \dot{A}^2}{4} = \frac{m_{s_{eff}} \dot{A}^2}{2}$$

$$m_{s_{eff}} = \frac{m_s}{2} = \left(\frac{1}{2}\right) \frac{7\rho\pi d^2 L}{32} = \frac{7\rho\pi d^2 L}{64} \tag{10}$$

Now, adding the correction term $m_{s_{eff}}$ to m_c in (6) gives:

$$\omega_n = \sqrt{\frac{k}{m_c + m_{s_{eff}}}} = \sqrt{\frac{\frac{384\pi E d^4}{343 L^3}}{\frac{\rho\pi d^2 L}{2} + \frac{7\rho\pi d^2 L}{64}}} = \sqrt{\frac{24576 E d^2}{13377 \rho L^4}} \tag{11}$$

2.1.2. Estimate of 2nd Critical Speed

The second mode of vibration for whirling is expected to involve tilting of the cylinder:
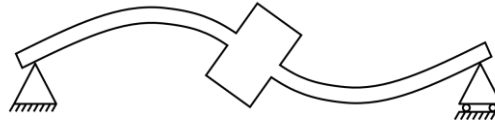
Figure 7: Second mode of vibration of rotor

2.1.2.1. Ignoring the Central Cylinder ($L \gg d$)

When the shaft is long and the diameter of the rotor is small, the effect of the central cylinder on the natural frequency is small, since it does not experience large

17

displacements. In this case an estimate of the whirling speed can be arrived at by ignoring the cylinder entirely, and by calculating the natural frequency corresponding to the second mode of lateral vibration of the shaft as a simply supported beam.

This is given by:

$$\omega_{2_s} = \frac{2^2 \pi^2}{L^2}\sqrt{\frac{EI}{\rho A}} = \frac{4\pi^2}{L^2}\sqrt{\frac{E\left(\frac{\pi d^4}{64}\right)}{\rho\left(\frac{\pi d^2}{4}\right)}} = \frac{\pi^2}{L^2}\sqrt{\frac{Ed^2}{\rho}} \tag{12}$$

2.1.2.2. Correcting for Tilting of Cylinder

In this bending vibration mode, the rotor can be thought to behave roughly like a system such as below:
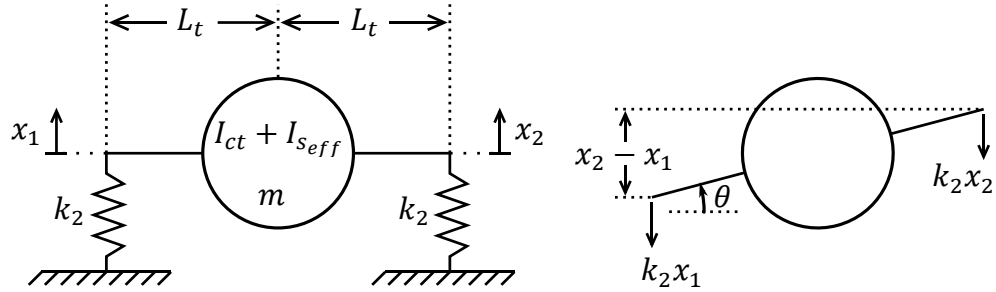
Figure 8: Discrete picture of second mode of bending vibration of rotor

Here, I_{ct} is the moment of inertia of the cylinder about its transverse axis and $I_{s_{eff}}$ is an additional effective moment of inertia due to the mass of the shaft.

The overall stiffness against net vertical displacement of the body is

$$k = 2k_2$$

This should be equal to the stiffness used for the first vibrational mode, from (5):

$$2k_2 = \frac{384E\pi d^4}{343L^3}$$

$$k_2 = \frac{192E\pi d^4}{343L^3} \tag{13}$$

Since deflections are small, the total counter clockwise moment on the body about its center is given by:

$$M_{ccw} = k_2 x_1 L_t - k_2 x_2 L_t = k_2 L_t (x_1 - x_2)$$

and this can be expressed in terms of the tilt θ of the body as:

$$M_{ccw} = 2k_2 L_t^2 \left(\frac{x_1 - x_2}{L_t}\right) = \left(2k_2 L_t^2\right)\theta \tag{14}$$

So, the system acts like a torsional oscillator with inertia $I_{ct} + I_{s_{eff}}$ and torsional stiffness

$$\kappa_t = 2k_2 L_t^2$$

The natural frequency is therefore

$$\omega_2 = \sqrt{\frac{\kappa_t}{I_{ct} + I_{s_{eff}}}} \tag{15}$$

κ_t here is the moment per unit angle required to tilt the middle of the rotor. Ignoring the central cylinder, the shaft behaves like a simply supported beam.
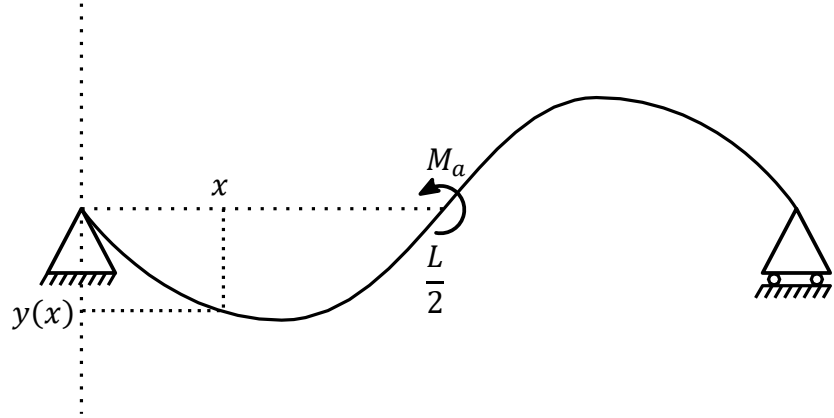
Figure 9: Profile of a simply supported beam in response to central perpendicular moment

Here, a simply supported beam of length l is subjected to a moment M_a at the mid-point. Between $x = 0$ and $x = \frac{l}{2}$, the beam is uniform and unloaded, so

$$EI y''''(x) = 0 \Rightarrow y''''(x) = 0$$

and $y(x)$ is a cubic polynomial:

$$y(x) = C_1 x^3 + C_2 x^2 + C_3 x + C4 \tag{16}$$

for some C_1, C_2 and C_3, and

$$y'(x) = 3C_1x^2 + 2C_2x + C_3 \tag{17}$$

and

$$y''(x) = 6C_1x + 2C_2 \tag{18}$$

Below are free-body diagrams of the beam and of the left half of the beam, including the point of application of M_a.
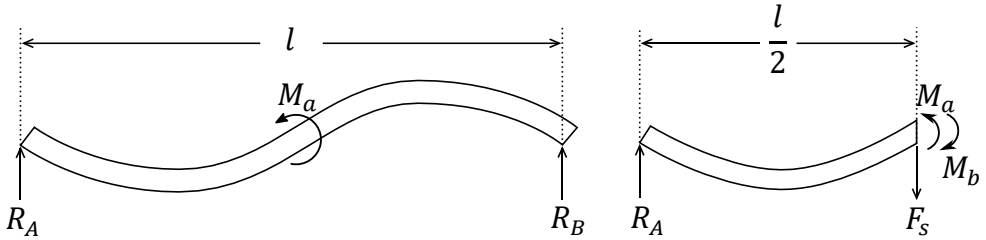
Figure 10: Free-body diagrams of simply supported beam and of a beam section

From moment balance about the right end of the beam,

$$M_a - R_A l = 0$$

$$R_A = \frac{M_a}{l} \tag{19}$$

Now, moment balance about the right end of the left half section of the beam gives

$$M_a - R_A \frac{l}{2} - M_b = 0$$

Substituting in R_A from (19),

$$M_b = M_a - \left(\frac{M_a}{l}\right)\frac{l}{2} = \frac{M_a}{2}$$

M_b is the bending moment in the beam at $x = \frac{l}{2}$, so

$$EIy''\left(\frac{l}{2}\right) = \frac{M_a}{2}$$

$$y''\left(\frac{l}{2}\right) = \frac{M_a}{2EI} \tag{20}$$

20

The bending moment at the left end of the beam is zero, so

$$EIy''(0) = 0 \Rightarrow y''(0) = 0 \tag{21}$$

At the left support,

$$y(0) = 0 \tag{22}$$

And at the mid-point of the shaft, by symmetry,

$$y\left(\frac{l}{2}\right) = 0 \tag{23}$$

Equations (20) through (23) are the boundary conditions for the left half of the beam and applying them to (16) through (18) gives

$$C_1 = \frac{M_a}{6EIl}, C_2 = 0, C_3 = -\frac{M_a l}{24EI}, C_4 = 0$$

So (17) becomes

$$y'(x) = \frac{M_a}{2EIl}x^2 - \frac{M_a l}{24EI}$$

and since deflections are small, the tilt in the middle of the beam is given by

$$\theta = y'\left(\frac{l}{2}\right) = \frac{M_a}{2EIL}\left(\frac{l}{2}\right)^2 - \frac{M_a l}{24EI} = M_a\left(\frac{l}{12EI}\right)$$

It is reasonable to take $l = \frac{7}{8}L$ since $\frac{1}{8}$ of the shaft does not bend significantly. Using this substitution, and the expression for I from (4), gives:

$$M_a = \left(\frac{12E\left(\frac{\pi d^4}{64}\right)}{\frac{7}{8}L}\right)\theta$$

$$M_a = \left(\frac{3}{14}\frac{\pi E d^4}{L}\right)\theta \tag{24}$$

and the effective moment per unit deflection required to tilt the middle of the beam is

$$\kappa_t = \left(\frac{3}{14} \frac{\pi E d^4}{L} \right) \tag{25}$$

The natural frequency of just the shaft without the central cylinder should now be

$$\omega_{2_s} = \sqrt{\frac{\kappa_t}{I_{s_{eff}}}} = \sqrt{\frac{\left(\frac{3}{14} \frac{\pi E d^4}{L} \right)}{I_{s_{eff}}}}$$

which means that the value of $I_{s_{eff}}$ can be found as

$$I_{s_{eff}} = \left(\frac{3}{14} \frac{\pi E d^4}{L} \right) \frac{1}{\omega_{2_s}^2} \tag{26}$$

Substituting in ω_{2_s} from (12),

$$I_{s_{eff}} = \left(\frac{3}{14} \frac{\pi E d^4}{L} \right) \frac{1}{\left(\frac{\pi^2}{L^2} \sqrt{\frac{E d^2}{\rho}} \right)^2} = \frac{3}{14} \left(\frac{L^3 d^2 \rho}{\pi^3} \right) \tag{27}$$

$I_{s_{eff}}$ includes the moment of inertia of the section of the shaft passing through the central cylinder. By the parallel axis theorem, then, I_{ct} is the moment of inertia of a solid cylinder of length $\frac{L}{8}$ and diameter $4d$ about its transverse axis, minus the moment of inertia of a solid cylinder of the same length and diameter d, also about its transverse axis:

$$I_{ct} = \left(\frac{1}{4} m_c \left(\frac{4d}{2} \right)^2 + \frac{1}{12} m_c \left(\frac{L}{8} \right)^2 \right)$$
$$- \left(\frac{1}{4} m_{is} \left(\frac{d}{2} \right)^2 + \frac{1}{12} m_{is} \left(\frac{L}{8} \right)^2 \right) \tag{28}$$

Where m_{is} is the mass of the section of shaft passing through the central cylinder and is given by density times volume:

$$m_{is} = \rho \times \frac{\pi d^2}{4} \times \frac{L}{8} = \frac{\rho \pi d^2 L}{32} \tag{29}$$

22

Substituting in m_c from (2) and m_{is} from (29) into (28) gives:

$$I_{ct} = \frac{255}{512}\rho\pi d^4 L + \frac{5}{8192}\rho\pi d^2 L^3 \tag{30}$$

Substituting κ_t, $I_{s_{eff}}$ and I_{ct} from equations (25), (27) and (28) into (15) gives

$$\omega_2 = \frac{32\pi^2 d}{7L}\sqrt{\frac{588E}{\rho(28560\pi^4 d^2 + 35\pi^4 L^2 + 12288L^2)}}$$

$$\approx 1094.06\left(\frac{d}{L}\right)\sqrt{\left(\frac{E}{\rho}\right)\left(\frac{1}{2782003.3d^2 + 15697.32L^2}\right)} \tag{31}$$

2.1.3. Rough Estimate of 3rd Critical Speed

The third mode of vibration for whirling is expected to primarily involve vibration of the shaft between the central cylinder and each support:
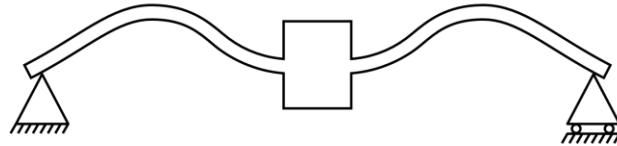
Figure 11: Third mode of vibration of rotor

Here, the central cylinder is expected to move much less than the shaft, so an estimate of the whirling speed can be arrived at by considering the vibration of half of the shaft with one end hinged and one end fixed:
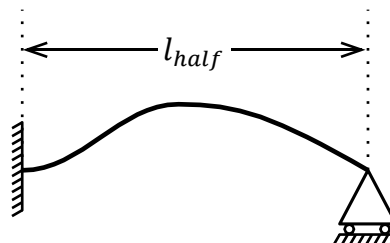
Figure 12: Approximation of shaft in third vibration mode

23

This behaves like a propped cantilever beam. Here, l_{half} is the length of the shaft to the right (or left) of the central cylinder, and is equal to $\frac{7}{16}L$.

Now we can use the expression for the natural frequency of a uniform beam:

$$\omega_{3_s} = \beta_1{}^2 \sqrt{\frac{EI}{\rho A}}$$

Where for a propped cantilever beam, the value of $\beta_1 l_{half}$ is taken to be 3.9266.
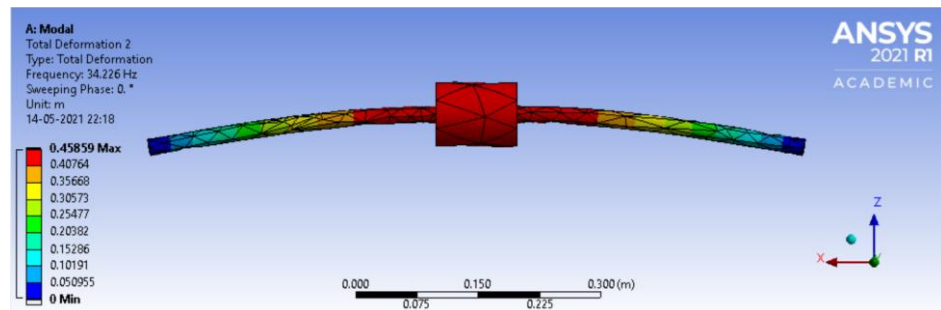
So, $\beta_1 = \frac{3.9266}{l_{half}}$ and

$$\omega_{3_s} = \left(\frac{3.9266}{l_{half}}\right)^2 \sqrt{\frac{E\left(\frac{\pi d^4}{64}\right)}{\rho\left(\frac{\pi d^2}{4}\right)}} = \left(\frac{16 \times 3.9266}{7 \times L}\right)^2 \sqrt{\frac{Ed^2}{16\rho}}$$

$$= \frac{20.1380}{L^2}\sqrt{\frac{Ed^2}{\rho}}$$

(32)

2.1.4. Ansys Results

The simulation takes $L = 0.8m$ and $d = 0.02m$. The material selection is cold drawn AISI 1045 Steel with $E = 2.05 \times 10^{11} Pa$ and $\rho = 7850 Kg/m^3$. The end faces of the rotor shaft are constrained in translation but free in rotation in all directions.

2.1.4.1. First Critical Speed

Two nearby modes are found at 34.266Hz and 34.445Hz.
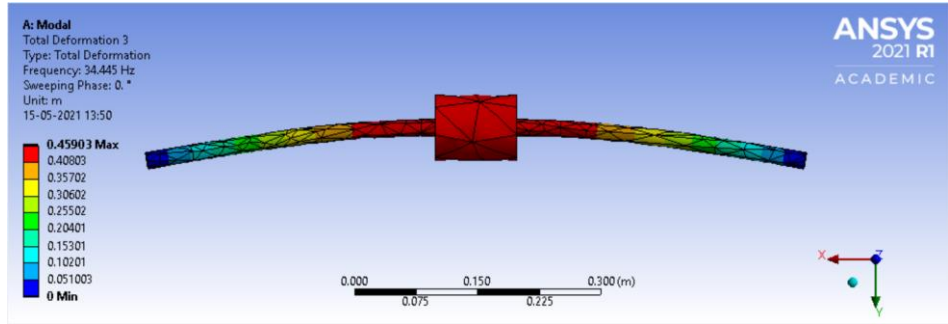
Figure 13: First bending mode found in Ansys

Comparison with the earlier calculation with these assumed values of L, d, E and ρ, and considering the shaft massless (eq. (6)) gives:

$$\omega_n = \sqrt{\frac{768Ed^2}{343\rho L^4}} = \sqrt{\frac{768 \times 2.05 \times 10^{11}Pa \times (0.02m)^2}{343 \times 7850Kg/m^3 \times (0.8m)^4}} = 238.960 \, rad/s$$

$$f_n = \frac{\omega_n}{2\pi} = 38.031Hz$$

And with the correction term for the mass of the shaft (eq. (11)), we have
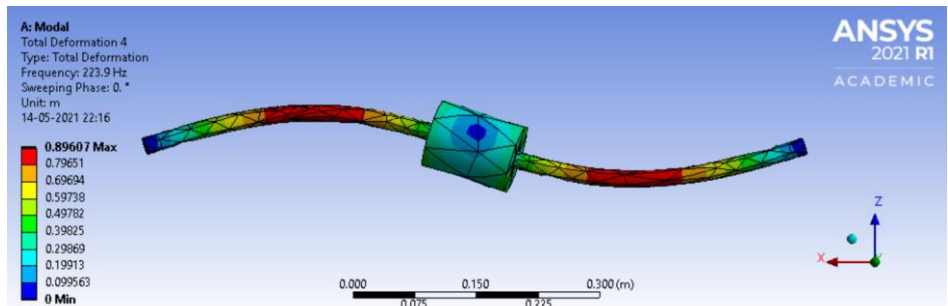
$$\omega_n = \sqrt{\frac{24576Ed^2}{13377\rho L^4}} = \sqrt{\frac{24576 \times 2.05 \times 10^{11}Pa \times (0.02m)^2}{13377 \times 7850Kg/m^3 \times (0.8m)^4}} = 216.455 \, rad/s$$

$$f_n = \frac{\omega_n}{2\pi} = 34.450Hz$$

This value agrees well with the Ansys result.

2.1.4.2. Second Critical Speed

Two nearby modes are found at 223.9Hz and 225.33Hz.
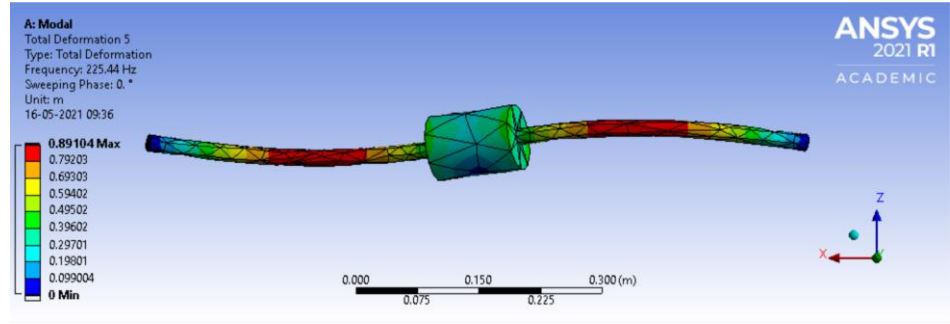
Figure 14: Second bending mode found in Ansys

Substituting values into expressions obtained for the second natural frequency by ignoring the cylinder (eq. (12)) gives

$$\omega_2 = \frac{\pi^2}{L^2}\sqrt{\frac{Ed^2}{\rho}} = \frac{\pi^2}{(0.8m)^2}\sqrt{\frac{2.05 \times 10^{11}Pa \times (0.02m)^2}{7850Kg/m^3}} = 1576.13rad/s$$

$$f_2 = \frac{\omega_2}{2\pi} = 250.85Hz$$

This value is about 12% off from the Ansys result.

With the correction term for the inertia of the cylinder (eq. (31)),

ω_2

$$= 1094.06\left(\frac{0.02m}{0.8m}\right)\sqrt{\left(\frac{2.05 \times 10^{11}Pa}{\frac{7850Kg}{m^3}}\right)\left(\frac{1}{2782003.3(0.02m)^2 + 15697.32(0.8m)^2}\right)}$$

$$= 1323.15rad/s$$

$$f_2 = 210.59Hz$$

This value is about 6% off from the Ansys result.

2.1.4.3. Third Critical Speed

A mode is found at 538.6Hz.
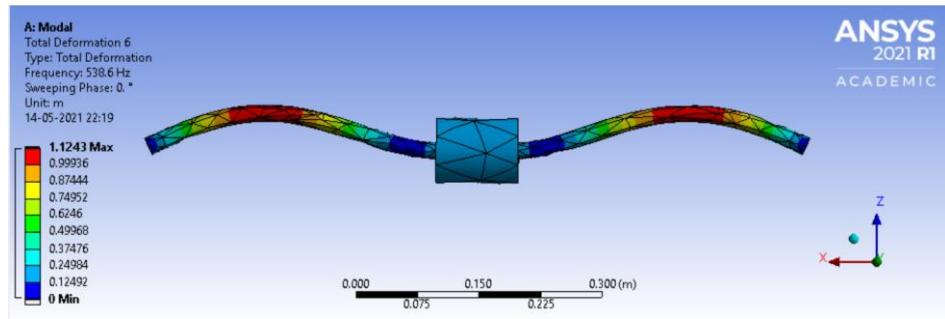
Figure 15: Third bending mode found in Ansys

Substituting values in (32) gives:

$$\omega_3 = \frac{20.1380}{L^2}\sqrt{\frac{Ed^2}{\rho}} = \frac{20.1380}{(0.8m)^2}\sqrt{\frac{2.05 \times 10^{11}Pa \times (0.02m)^2}{7850Kg/m^3}} = 3215.94\,rad/s$$

$$f_3 = \frac{\omega_3}{2\pi} = 511.83Hz$$

This value is about 5% off from the Ansys result.

2.2. Effect of Non-Terminal Support Placement

A rotor consisting of a long shaft with a concentric cylinder mounted midway is simply supported at equal distances from each end, as shown below. The goal is to arrive at an expression for the natural frequency of bending vibration of the system and verify the results using simulation in Ansys.
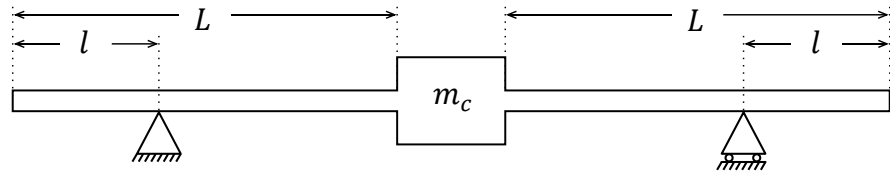
Figure 16: Rotor being considered

2.2.1. Analytical Method

As seen in Figure 16, the length of the shaft on either side of the central cylinder is L and the supports are at l from either end. The central cylinder has mass m_c and the shaft has linear mass density ρA.

Calculation of all natural frequencies of the system is possible given L, l and other parameter values, through solution of an eigenvalue problem derived from Partial Differential Equations governing beam vibration for sections of the shaft on either side of each support, with zero shear and bending at the free end, imposed continuity of slope and curvature at the support, and shear force equal, by symmetry, to $\frac{m_c}{2}$ times the vertical acceleration at the point of the shaft-cylinder interface. However, this leads to complicated transcendental equations involving all system parameters and does not easily yield a simple expression for natural frequency in terms of L and l.

The approach taken here is to estimate the first natural frequency of the system by modelling it as a spring-mass system of stiffness k equal to the lateral stiffness of the shaft, and mass $m_c + m_{s_{eff}}$ where $m_{s_{eff}}$ is an effective equivalent mass of the shaft at its center.

28
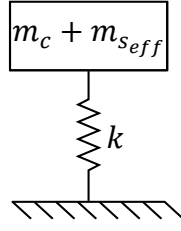
Figure 17: Spring-mass picture of rotor for bending vibrations

The natural frequency, then, is given by

$$\omega_n = \sqrt{\frac{k}{m_c + m_{s_{eff}}}}$$ (33)

The lateral deflection of the beam in response to a static load at the center is unaffected by any overhang of the shaft beyond the supports. Since the section of the shaft passing through the central cylinder experiences no significant bending, the effective length of the shaft for the purposes of determination of static deflection is $2(L - l)$.
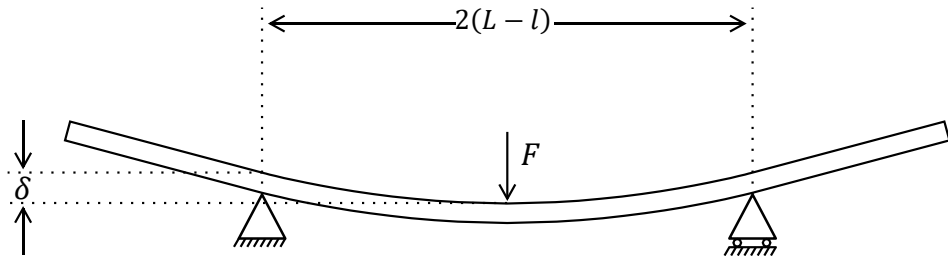
Figure 18: Deflection of shaft in response to lateral load at mid-point

The deflection of the shaft as a simply supported beam is therefore given by

$$\delta = \frac{F\big(2(L-l)\big)^3}{48EI}$$

and the stiffness is

$$k = \frac{F}{\delta} = \frac{6EI}{(L-l)^3}$$ (34)

The profile of the shaft at any time t is approximated as a cubic polynomial $y(x)$ times some function $D(t)$ chosen such that the coefficient of x^3 in $y(x)$ is 1.
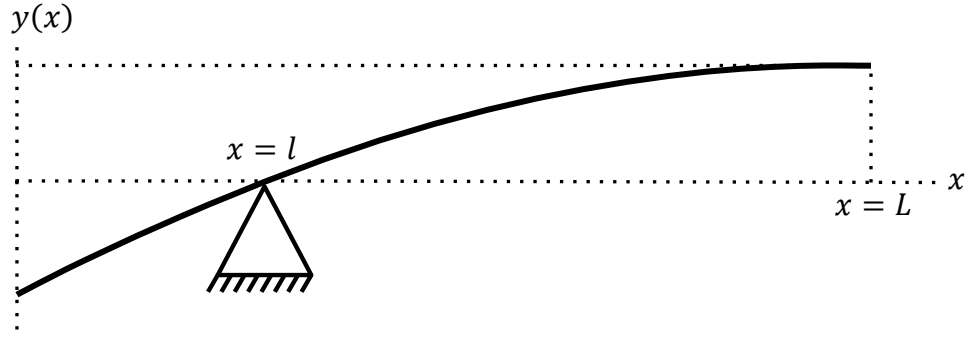
Figure 19: Profile of half of shaft during bending vibration of rotor

The assumed shape of the beam is

$$y(x) = x^3 + C_1 x^2 + C_2 x + C_3 \tag{35}$$

for some C_1, C_2, and C_3.

So,

$$y'(x) = 3x^2 + 2C_1 x + C_2 \tag{36}$$

$$y''(x) = 6x + 2C_1 \tag{37}$$

At $x = 0$, the end of the beam is free, so the bending moment in the beam is zero

$$EIy''(0) = 0 \Rightarrow y''(0) = 0 \tag{38}$$

At the support, the displacement is zero

$$y(l) = 0 \tag{39}$$

At the shaft-cylinder interface, the shaft is parallel to the cylinder, which is horizontal by symmetry.

$$y'(L) = 0 \tag{40}$$

Applying (38) through (40) to (35) through (37) gives:

$$C_1 = 0, C_2 = -3L^3, C_3 = -l^3 + 3L^2 l$$

30

Substituting this back into (35),

$$y(x) = x^3 - 3L^2x - l^3 + 3L^2l \tag{41}$$

Now, the kinetic energy in length dx of the beam at position x and time t is given by

$$KE_x = \frac{1}{2} \times (\rho A dx) \times \left(\frac{\partial\left(D(t)y(x)\right)}{\partial t}\right)^2$$

$$KE_x = \frac{1}{2} \times (\rho A dx) \times \left(\dot{D}(t)\right)^2 (y(x))^2$$

So, the total kinetic energy in half of the beam is

$$\frac{KE}{2} = \int_0^L \frac{1}{2} \rho A \left(\dot{D}(t)\right)^2 (y(x))^2 dx$$

Substituting $y(x)$ in from (41), integrating and multiplying through by 2 gives the total kinetic energy in the beam as

$$KE = \rho A \left(\dot{D}(t)\right)^2 \left(\frac{68}{35}L^7 + \frac{5}{2}L^4l^3 - \frac{15}{2}L^6l + Ll^6 - 6L^3l^4 \right.$$
$$\left. + 9L^5l^2\right) \tag{42}$$

The kinetic energy due to an effective mass $m_{s_{eff}}$ at $x = L$ would be given by

$$KE = \frac{1}{2} \times m_{s_{eff}} \times \left(\frac{\partial\left(D(t)y(L)\right)}{\partial t}\right)^2$$

$$KE = \frac{1}{2} \times m_{s_{eff}} \times \left(\dot{D}(t)\right)^2 (y(L))^2$$

Using (41) to evaluate $y(L)$ gives:

$$KE = \frac{1}{2} \times m_{s_{eff}}$$
$$\times \left(\dot{D}(t)\right)^2 (4L^6 + 4L^3l^3 - 12L^5l + l^6 - 6L^2l^4 \tag{43}$$
$$+ 9L^4l^2)$$

Equating KE from (42) and (43) gives

31

$$\frac{m_{S_{eff}}}{2}(4L^6 + 4L^3l^3 - 12L^5l + l^6 - 6L^2l^4 + 9L^4l^2)$$

$$= \rho A\left(\frac{68}{35}L^7 + \frac{5}{2}L^4l^3 - \frac{15}{2}L^6l + Ll^6 - 6L^3l^4 + 9L^5l^2\right)$$

Which gives $m_{S_{eff}}$ as

$$m_{S_{eff}}$$
$$= \rho AL\left(\frac{136L^6 + 175L^3l^3 - 525L^5l + 70l^6 - 420L^2l^4 + 630L^4l^2}{140L^6 + 140L^3l^3 - 420L^5l + 35l^6 - 210L^2l^4 + 315L^4l^2}\right) \tag{44}$$

(44) can be expanded into partial fractions as

$$m_{S_{eff}} = \rho AL\left(\frac{34}{35} + \frac{2567}{2835}\left(\frac{l}{L-l}\right) + \frac{47}{63}\left(\frac{l}{L-l}\right)^2\right.$$
$$+ \frac{44}{45}\left(\frac{l}{L-l}\right)^3 + \frac{22}{105}\left(\frac{l}{L-l}\right)^4 + \frac{113}{810}\left(\frac{l}{2L+l}\right)$$
$$\left. + \frac{11}{1890}\left(\frac{l}{2L+l}\right)^2\right) \tag{45}$$

If R is the ratio of overhung length to supported length of half the shaft, that is

$$R = \frac{l}{L-l} \tag{46}$$

Then

$$\frac{l}{2L+l} = \frac{R}{2+3R} \tag{47}$$

and (45) can be written as

$$m_{S_{eff}} = \rho AL\left(\frac{34}{35} + \frac{2567}{2835}R + \frac{47}{63}R^2 + \frac{44}{45}R^3 + \frac{22}{105}R^4\right.$$
$$\left. + \frac{113}{810}\left(\frac{R}{2+3R}\right) + \frac{11}{1890}\left(\frac{R}{2+3R}\right)^2\right) \tag{48}$$

(46) can be rewritten as

$$l = \frac{RL}{R+1}$$

Substituting this expression for l into (34) gives

$$k = \frac{6EI(R+1)^3}{L^3} \tag{49}$$

From (49), (45) and (33), the expression for natural frequency becomes

$$\omega_n = \sqrt{\frac{6EI(R+1)^3}{L^3\left(m_c + \rho AL\left(\frac{34}{35} + \frac{2567}{2835}R + \frac{47}{63}R^2 + \frac{44}{45}R^3 + \frac{22}{105}R^4 + \frac{113}{810}\left(\frac{R}{2+3R}\right) + \frac{11}{1890}\left(\frac{R}{2+3R}\right)^2\right)\right)}} \tag{50}$$

Where EI is the flexural rigidity of the shaft, L is the total length of the shaft on either side of the central cylinder, R is the ratio of overhung to supported shaft length on either side of the central cylinder, m_c is the mass of the central cylinder, and ρA is the linear mass density of the shaft.

2.2.2. Comparison with Ansys Results

The simulation uses a steel ($\rho = 7850 \ Kg/m^3$, $E = 2.05 \times 10^{11} \ Pa$) rotor consisting of a central cylinder of diameter $0.08 \ m$ and length $0.1 \ m$. The shaft length on either side of the central cylinder is $L = 0.35 \ m$ and the diameter of the shaft is $0.02 \ m$.

The mass of the central cylinder is therefore

$$m_c = 7850 \ Kgm^{-3} \times \frac{\pi(0.08 \ m)^2}{4} \times 0.1 \ m = 3.9458 \ Kg$$

The flexural rigidity of the shaft is

$$EI = 2.05 \times 10^{11} \ Pa \times \frac{\pi(0.02 \ m)^4}{64} = 1610.0662 \ Nm^2$$

and the linear mass density of the shaft is

$$\rho A = 7850 \ Kgm^{-3} \times \frac{\pi(0.02 \ m)^2}{4} = 2.46615 \ Kgm^{-1}$$

2.2.2.1. Case 1: $R = \frac{1}{6}$

The bearings in the simulation are placed $50\ mm$ from either end.

So, $R = \frac{50\ mm}{350\ mm - 50\ mm} = \frac{1}{6}$.

Substituting parameter values into (50) gives $\omega_n = 269\ rad\ s^{-1}$, so $f_n = 42.81\ Hz$.

The first nonzero natural frequency found in the simulation is $45.85\ Hz$.
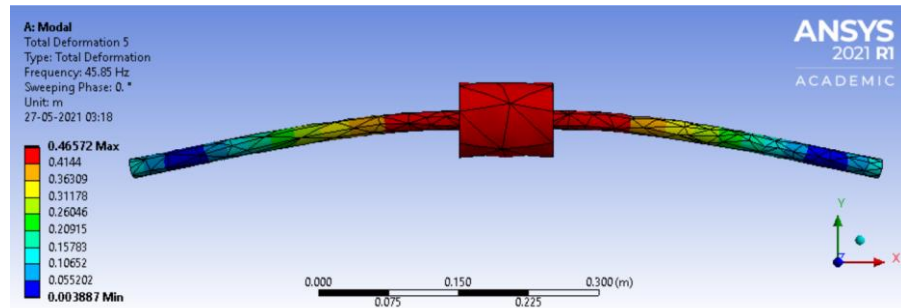
Figure 20: First mode found for R=1/6

The estimated value was about 6% off from the simulation.

2.2.2.2. Case 2: $R = \frac{2}{5}$

The bearings are placed $100\ mm$ from either end.

Substituting parameter values into (50) gives $\omega_n = 342.4\ rad\ s^{-1}$, so $f_n = 54.49\ Hz$.

The first nonzero natural frequency found in the simulation is $57.263\ Hz$.
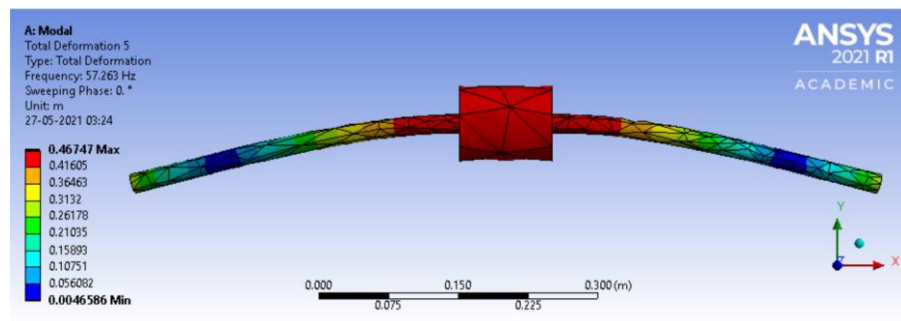
Figure 21: First mode found for R=2/5

The estimated value was about 5% off from the simulation.

2.2.2.3. Case 3: $R = \frac{3}{4}$

The bearings are placed $150\ mm$ from either end.

Substituting parameter values into (50) gives $\omega_n = 442.49\ rad\ s^{-1}$, so $f_n = 70.42\ Hz$.

The first nonzero natural frequency found in the simulation is $74.656\ Hz$.
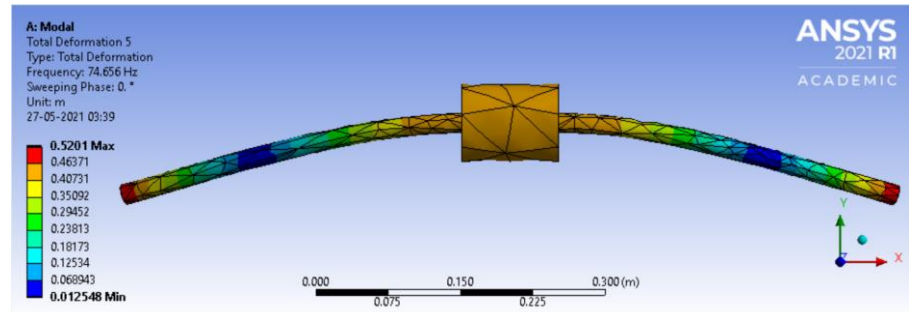
Figure 22: First mode found for R=3/4

The estimated value was about 5% off from the simulation.

3. QUALITATIVE DESCRIPTION OF THE CORIOLIS EFFECT ON ROTORS

The so-called Coriolis effect or gyroscopic effect is what separates problems in rotor dynamics from general vibration problems. Since rotor whirl is commonly seen as bending vibration superimposed on a spinning motion, a common approach to model rotors is to write equations from a reference frame that is either attached to the rotor or is spinning with it. Such a reference frame, however, is necessarily non-inertial, meaning that in it the rotor will be seen to experience perceived inertial forces. The broad effect of such forces on the rotor's vibrational behaviour is generally to raise or lower the natural frequency of the system, or to stabilize or de-stabilize particular vibrational modes. This section of the thesis presents illustrative examples of how Coriolis terms affect rotor whirl at a fundamental level.

3.1. Coriolis Acceleration

The Coriolis term is one of five terms in the five-term acceleration formula, which is an expression for the acceleration as seen in an inertial frame of an object whose velocity and acceleration are known in a non-inertial frame.

The figure below shows a non-inertial reference frame xyz spinning with angular velocity $\vec{\omega}$ about its origin B located at $\vec{R}$, where $\vec{\omega}$ and $\vec{R}$ are measured in the inertial reference frame XYZ with its origin at A.
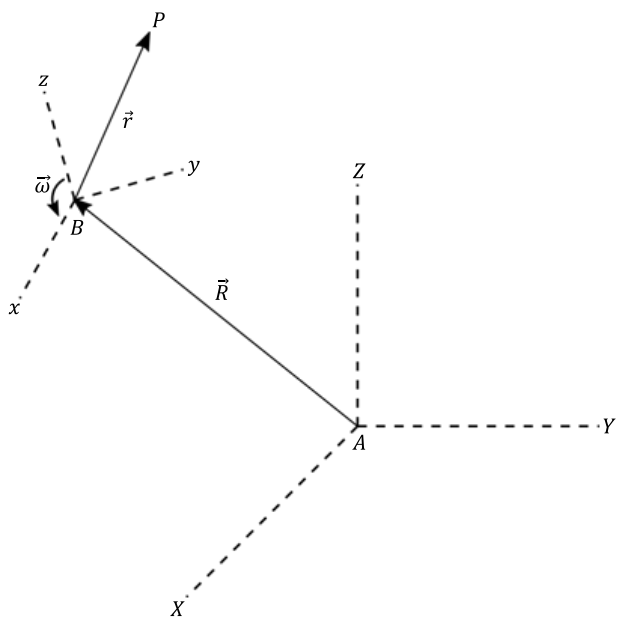
Figure 23: Inertial and non-inertial reference frame and position vector of an object

$\vec{r}$ is the position vector relative to B of an object P. The velocity of P as seen in xyz is taken to be $\dot{\vec{r}}_{xyz} = v_{relative}$. Relative to A, P is at $(\vec{R} + \vec{r})$ and its velocity as seen in XYZ is

$$\vec{v} = \left[\frac{d(\vec{R} + \vec{r})}{dt}\right]_{XYZ} = \left[\frac{d(\vec{R})}{dt}\right]_{XYZ} + \left[\frac{d(\vec{r})}{dt}\right]_{xyz} + \vec{\omega} \times \vec{r}$$

$$\vec{v} = \dot{\vec{R}}_{XYZ} + \dot{\vec{r}}_{xyz} + \vec{\omega} \times \vec{r}$$

Differentiating this with respect to time gives

$$\left[\frac{d(\vec{v})}{dt}\right]_{XYZ} = \left[\frac{d\left(\dot{\vec{R}}\right)}{dt}\right]_{XYZ} + \left[\frac{d(\dot{\vec{r}} + \vec{\omega} \times \vec{r})}{dt}\right]_{xyz} + \vec{\omega} \times (\dot{\vec{r}}_{xyz} + \vec{\omega} \times \vec{r})$$

$$\dot{\vec{v}}_{XYZ} = \ddot{\vec{R}}_{XYZ} + \ddot{\vec{r}}_{xyz} + \dot{\vec{\omega}}_{XYZ} \times \vec{r} + \vec{\omega} \times \dot{\vec{r}}_{xyz} + \left(\vec{\omega} \times (\dot{\vec{r}}_{xyz} + \vec{\omega} \times \vec{r})\right)$$

$$\dot{\vec{v}}_{XYZ} = \ddot{\vec{R}}_{XYZ} + \ddot{\vec{r}}_{xyz} + \dot{\vec{\omega}}_{XYZ} \times \vec{r} + \vec{\omega} \times \dot{\vec{r}}_{xyz} + \vec{\omega} \times \dot{\vec{r}}_{xyz} + \vec{\omega} \times (\vec{\omega} \times \vec{r})$$

$$\dot{\vec{v}}_{XYZ} = \ddot{\vec{R}}_{XYZ} + \ddot{\vec{r}}_{xyz} + \dot{\vec{\omega}}_{XYZ} \times \vec{r} + 2\vec{\omega} \times \dot{\vec{r}}_{xyz} + \vec{\omega} \times (\vec{\omega} \times \vec{r})$$

This can be rewritten as

$$\vec{a} = \vec{a}_{frame} + \vec{a}_{relative} + \vec{\alpha} \times \vec{r} + 2\vec{\omega} \times \vec{v}_{relative} + \vec{\omega} \times (\vec{\omega} \times \vec{r}) \tag{51}$$

Where $\vec{a}$ is the acceleration of an object as seen in an inertial reference frame, $\vec{a}_{frame}$ is the acceleration of a non-inertial reference frame as seen from the inertial reference frame, $\vec{a}_{relative}$ is the acceleration of the object as seen in the non-inertial reference frame, $\vec{\alpha}$ is the angular acceleration of the non-inertial reference frame, $\vec{r}$ is the position of the object relative to the origin of the non-inertial reference frame (about which point the non-inertial reference frame is spinning) and $\vec{v}_{relative}$ is the velocity of the object as seen in the non-inertial reference frame.

Equation (51) is the five-term acceleration formula and $2\vec{\omega} \times \vec{v}_{relative}$ is called the Coriolis term. It corresponds to an acceleration experienced by an object moving at a constant velocity relative to a rotating reference frame. This acceleration is in a

direction perpendicular to the velocity of the object and to the angular velocity of the reference frame as seen from an inertial reference frame.

So:

$$\overrightarrow{\text{Coriolis acceleration of object}}$$
$$= 2\left(\overrightarrow{\text{angular velocity of frame}} \times \overrightarrow{\text{velocity of object in frame}}\right)$$

(52)

3.2. Coriolis Effect on Whirling Rotor: Reference Frames

The case considered for the following is that of near-steady asynchronous whirl. A rotor spins at angular velocity ω and whirls at angular velocity Ω, where ω and Ω are both measured in the inertial lab reference frame XYZ.
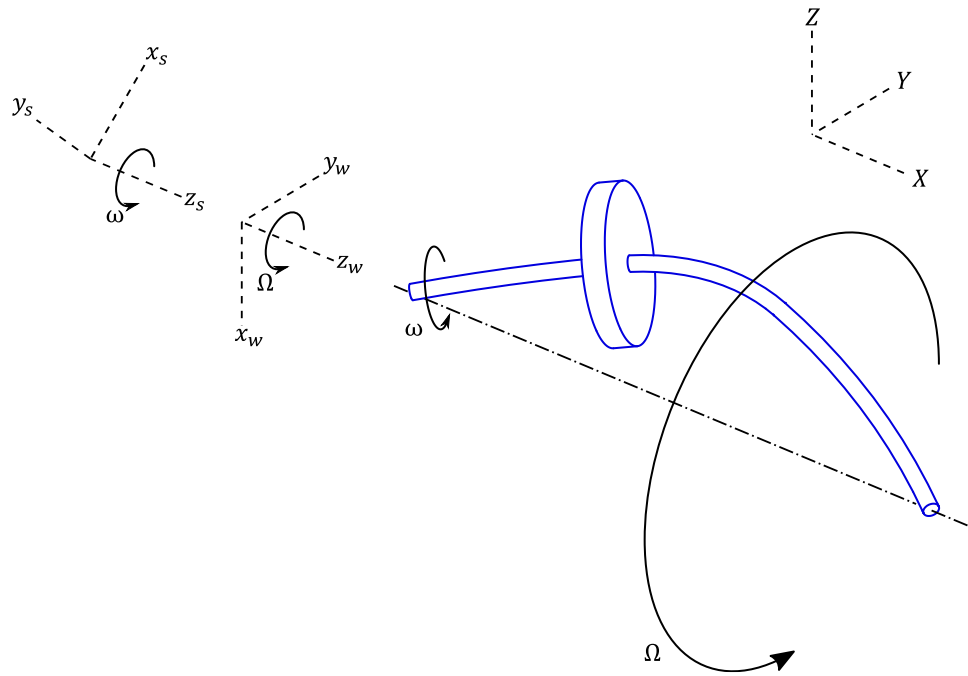
Figure 24: Rotor spinning at ω and whirling at Ω in inertial reference frame XYZ

Two different non-inertial reference frames are now considered:

Non-inertial reference frame $x_s y_s z_s$ is attached to the nominal (undeformed) axis of the rotor, and rotates about this axis at ω, i.e. at the spin speed of the rotor. In this frame, the rotor is observed to orbit the nominal axis at $(\Omega - \omega)$ without spinning.

Non-inertial reference frame $x_w y_w z_w$ is attached to the nominal axis and rotates about it at Ω, i.e. at the whirl speed of the rotor. In this frame, the rotor is observed to spin at $(\omega - \Omega)$ with a constant deflection in a fixed direction, but with no whirl.

3.3. Coriolis Effect in the Spin-Synchronized Frame

The rotor is shown below as seen in reference frame $x_s y_s z_s$.
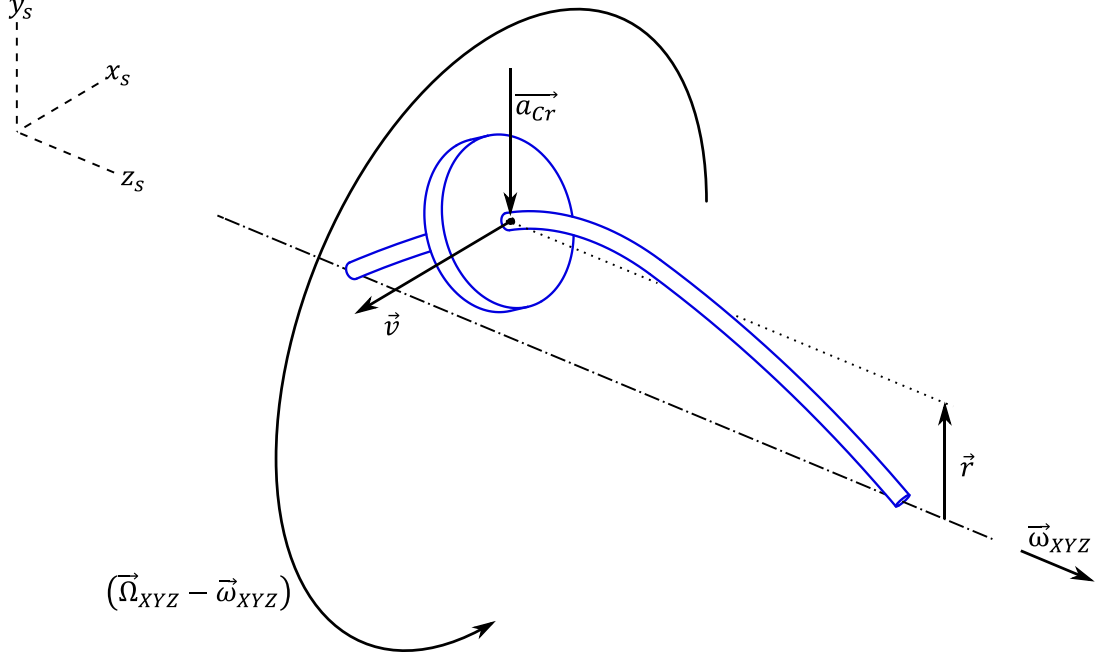
Figure 25: Whirling rotor as seen in reference frame $x_s y_s z_s$

Since in $x_s y_s z_s$ the rotor orbits at $\left(\vec{\Omega}_{XYZ} - \vec{\omega}_{XYZ}\right)$ but does not spin, the velocity of any point at $\vec{r}$ relative to the nominal axis is given by

$$\vec{v} = \left(\vec{\Omega}_{XYZ} - \vec{\omega}_{XYZ}\right) \times \vec{r} \tag{53}$$

Since $\left(\vec{\Omega}_{XYZ} - \vec{\omega}_{XYZ}\right)$ is in the axial direction and $\vec{r}$ is radial, $\vec{v}$ is tangential to the rotor.

Since the frame is rotating with angular velocity $\vec{\omega}_{XYZ}$, the Coriolis term of acceleration is:

$$\overrightarrow{a_{Cr}} = 2\vec{\omega}_{XYZ} \times \vec{v}$$

Which is in the radial direction, since $\vec{\omega}_{XYZ}$ is axial and $\vec{v}$ is tangential. Using (53), this becomes

$$\overrightarrow{a_{Cr}} = 2\vec{\omega}_{XYZ} \times \left(\left(\vec{\Omega}_{XYZ} - \vec{\omega}_{XYZ} \right) \times \vec{r} \right) \tag{54}$$

In $x_s y_s z_s$, the Coriolis effect manifests as an inertial force in the opposite direction as the Coriolis acceleration,

$$\overrightarrow{F_{Cr}} = -m_r \overrightarrow{a_{Cr}}$$

Where m_r has units of mass. Using (54), this becomes

$$\overrightarrow{F_{Cr}} = 2m_r \vec{\omega}_{XYZ} \times \left(\left(\vec{\omega}_{XYZ} - \vec{\Omega}_{XYZ} \right) \times \vec{r} \right) \tag{55}$$

In $x_s y_s z_s$, then, the Coriolis effect causes a perceived force on the rotor in the radial direction, given by (55).

3.4.   Coriolis Effect in the Whirl-Synchronized Frame

The rotor is shown below as seen in reference frame $x_w y_w z_w$.
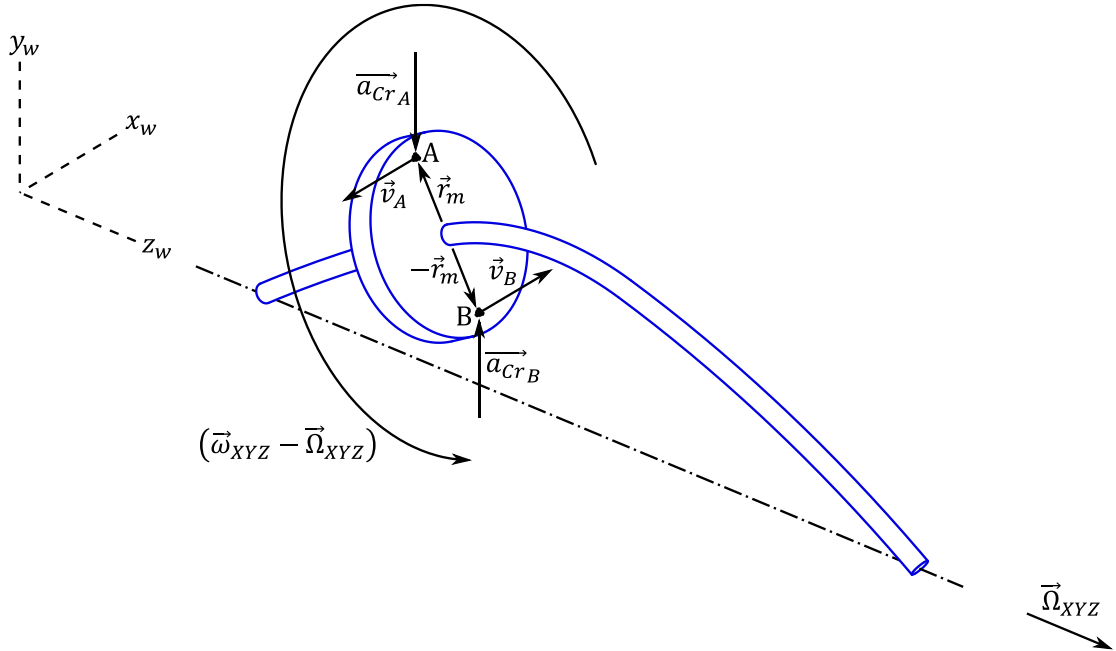
Figure 26: Whirling rotor as seen in non-inertial frame $x_w y_w z_w$

A and B are two material points, chosen to lie at equal distances from the actual (deformed) axis of the rotor along the same diameter. They are taken to be at $\vec{r}_m$ and $-\vec{r}_m$ relative to the deformed axis of the rotor.

Since in $x_w y_w z_w$ the rotor spins about the deformed axis with angular velocity $\left(\vec{\omega}_{XYZ} - \vec{\Omega}_{XYZ}\right)$ but does not whirl, the velocities of A and B are given by

$$\vec{v}_A = \left(\vec{\omega}_{XYZ} - \vec{\Omega}_{XYZ}\right) \times \vec{r}_m \tag{56}$$

$$\vec{v}_B = \left(\vec{\omega}_{XYZ} - \vec{\Omega}_{XYZ}\right) \times -\vec{r}_m$$

$$\vec{v}_B = -\left(\vec{\omega}_{XYZ} - \vec{\Omega}_{XYZ}\right) \times \vec{r}_m \tag{57}$$

Since the frame is rotating with angular velocity $\vec{\Omega}_{XYZ}$, the Coriolis accelerations of A and B are given by

$$\vec{a_{Cr}}_A = 2\vec{\Omega}_{XYZ} \times \vec{v}_A$$

which, using (56), becomes

$$\vec{a_{Cr}}_A = 2\vec{\Omega}_{XYZ} \times \left(\left(\vec{\omega}_{XYZ} - \vec{\Omega}_{XYZ}\right) \times \vec{r}_m\right) \tag{58}$$

and

$$\vec{a_{Cr}}_B = 2\vec{\Omega}_{XYZ} \times \vec{v}_B$$

which, using (57), becomes

$$\vec{a_{Cr}}_B = -2\vec{\Omega}_{XYZ} \times \left(\left(\vec{\omega}_{XYZ} - \vec{\Omega}_{XYZ}\right) \times \vec{r}_m\right) \tag{59}$$

In $x_w y_w z_w$, Coriolis effects at A and B manifest as inertial forces in directions opposite to those of the Coriolis accelerations. Using (58) and (59),

$$\vec{F_{Cr}}_A = -m\left(2\vec{\Omega}_{XYZ} \times \left(\left(\vec{\omega}_{XYZ} - \vec{\Omega}_{XYZ}\right) \times \vec{r}_m\right)\right) \tag{60}$$

$$\vec{F_{Cr}}_B = m\left(2\vec{\Omega}_{XYZ} \times \left(\left(\vec{\omega}_{XYZ} - \vec{\Omega}_{XYZ}\right) \times \vec{r}_m\right)\right) \tag{61}$$

Where m has units of mass.

Since A and B are separated by $\left(\vec{r}_m - (-\vec{r}_m)\right) = 2\vec{r}_m$, and since $\overrightarrow{F_{Cr_A}} = -\overrightarrow{F_{Cr_B}}$, Coriolis terms at A and B give rise to a net perceived moment on the rotor:

$$\overrightarrow{M_{Cr}} = 2\vec{r}_m \times \overrightarrow{F_{Cr_A}} = -2\vec{r}_m \times \overrightarrow{F_{Cr_B}}$$

$$\overrightarrow{M_{Cr}} = 2\vec{r}_m \times \left(-m\left(2\vec{\Omega}_{XYZ} \times \left((\vec{\omega}_{XYZ} - \vec{\Omega}_{XYZ}) \times \vec{r}_m\right)\right)\right)$$

$$\overrightarrow{M_{Cr}} = -4m\vec{r}_m \times \left(\vec{\Omega}_{XYZ} \times \left((\vec{\omega}_{XYZ} - \vec{\Omega}_{XYZ}) \times \vec{r}_m\right)\right)$$

Using the identity $\vec{A} \times (\vec{B} \times \vec{C}) = (\vec{A} \cdot \vec{C})\vec{B} - (\vec{A} \cdot \vec{B})\vec{C}$, this becomes

$$\overrightarrow{M_{Cr}} = -4m\vec{r}_m \times \left((\vec{\Omega}_{XYZ} \cdot \vec{r}_m)(\vec{\omega}_{XYZ} - \vec{\Omega}_{XYZ}) - \left(\vec{\Omega}_{XYZ} \cdot (\vec{\omega}_{XYZ} - \vec{\Omega}_{XYZ})\right)\vec{r}_m\right)$$

$$\overrightarrow{M_{Cr}} = -4m\left((\vec{\Omega}_{XYZ} \cdot \vec{r}_m)\left(\vec{r}_m \times (\vec{\omega}_{XYZ} - \vec{\Omega}_{XYZ})\right)\right.$$
$$\left. - \left(\vec{\Omega}_{XYZ} \cdot (\vec{\omega}_{XYZ} - \vec{\Omega}_{XYZ})\right)(\vec{r}_m \times \vec{r}_m)\right)$$

and $\vec{r}_m \times \vec{r}_m$ is zero, so

$$\overrightarrow{M_{Cr}} = -4m(\vec{\Omega}_{XYZ} \cdot \vec{r}_m)\left(\vec{r}_m \times (\vec{\omega}_{XYZ} - \vec{\Omega}_{XYZ})\right) \tag{62}$$

$(\vec{\omega}_{XYZ} - \vec{\Omega}_{XYZ})$ is along the nominal axis of the rotor, and the perceived moment $\overrightarrow{M_{Cr}}$ is perpendicular to it. $\overrightarrow{M_{Cr}}$, therefore, acts to tilt the rotor as seen in $x_w y_w z_w$.

3.5. Inferences

From Figures 25 and 26, and equations (55) and (62), it is evident that the physical interpretation of the effects of Coriolis/gyroscopic terms is dependent on the choice of reference frame. It is also clear that when $(\omega - \Omega) = 0$, i.e. in the case of synchronous whirl, Coriolis terms do not appear in reference frames which are rotating at the spin or whirl speeds of the rotor about its nominal axis. Moreover, if the rotor, due to symmetry or other reasons, does not tilt, then $\left(\vec{\Omega} \cdot \vec{r}_m \right)$ goes to zero in equation (62) and gyroscopic moments do not act on the rotor. Lastly, it can be seen that changing the sign of $(\omega - \Omega)$ reverses the direction of perceived forces or moments due to Coriolis terms in the reference frames considered. Such effects can therefore act either to increase or decrease the deflection or tilt of the rotor.

4.   A FULLY ANALYTICAL WHIRL CALCULATION

A Campbell diagram plots the change in the natural frequencies of a rotor system as the imposed spin speed changes. Unlike with the approximations presented thus far, plotting a Campbell diagram requires a correct accounting of the effects of spin. The following is a Newtonian formulation for a simple rotor treated as a rigid disc on a thin shaft. The goal is to use analytical methods to plot a Campbell diagram and compare it with the Campbell diagram obtained from simulation in Ansys.

A rotor consisting of a $100mm$ long cylinder of diameter $80mm$ mounted midway on a shaft of length $800mm$ and diameter $20mm$ has been considered in earlier exercises. Here, the length of the central cylinder has been reduced to $20mm$ to make it better suited to thin-disc treatments. The density of the disc has been increased so as to keep the mass of the rotor the same as before. The dimensions of the rotor are as shown below.
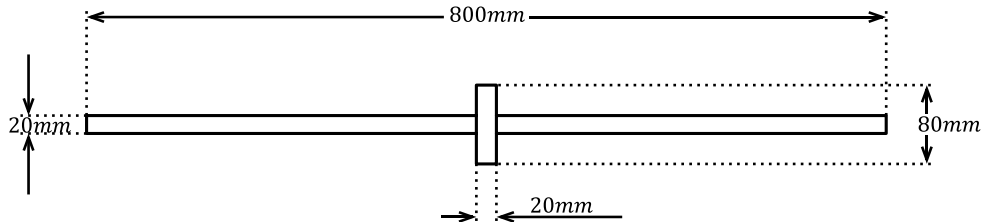
Figure 27: Dimensions of the rotor

4.1.   Physical Properties of the Rotor

As in previous exercises, the material selection for the shaft in Ansys is cold drawn AISI 1045 Steel with $E = 2.05 \times 10^{11} Pa$ and $\rho = 7850 Kg/m^3$.

Since the mass of the disc is intended to remain unchanged despite a reduction of its length by a factor of five ($100mm$ to $20mm$), the density of the disc is increased by a factor of five. Therefore, $\rho_{disc} = 7850 Kg/m^3 \times 5 = 39250 Kg/m^3$.

The linear mass density of the shaft is

$$\rho A = 7850 Kg/m^3 \ \times \frac{\pi \times (0.02m)^2}{4} = 2.466 Kg/m \tag{63}$$

and its flexural rigidity is

$$EI = 2.05 \times 10^{11} Pa \times \frac{\pi \times (0.02m)^4}{64} = 1610.07 Nm^2 \tag{64}$$
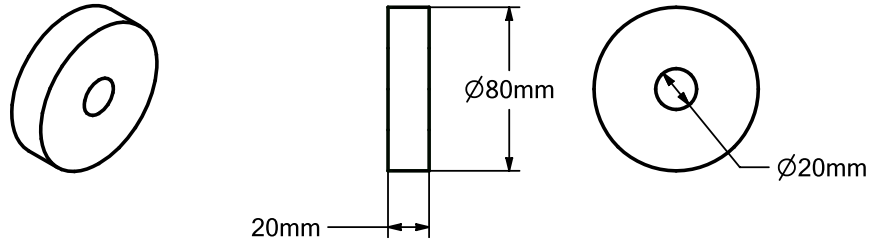
Figure 28: Dimensions of the central disc on the rotor

The mass of the disc is given by its density times its volume:

$$m = 39250 Kg/m^3 \times \frac{\pi \times ((0.08m)^2 - (0.02m)^2)}{4} \times 0.02m \tag{65}$$
$$= 3.699 Kg$$

The axial mass moment of inertia of the disc is

$$J_{axial} = \frac{\pi}{32} \rho_{disc} l_{disc} (D_{outer}^4 - D_{inner}^4)$$

Substituting appropriate values, this gives

$$J_{axial} = 3.144 \times 10^{-3} Kgm^2 \tag{66}$$

The transverse mass moment of inertia is

$$J_{transverse} = \frac{\pi}{192} \rho_{disc} l_{disc} (D_{outer}^2 - D_{inner}^2)(3(D_{outer}^2 + D_{inner}^2) + 4L_{disc}^2)$$

Substituting appropriate values, this gives

$$J_{transverse} = 1.695 \times 10^{-3} Kgm^2 \tag{67}$$

4.2. Analytical Treatment

The approach used here involves incorporating the bending moments and shear forces responsible for causing the linear and angular acceleration of the spinning disc as boundary conditions into a beam vibration problem.

4.2.1. Assumptions

The analysis performed here assumes a fixed coordinate system where the nominal spin of the rotor is about the x axis. The gyroscopic effects due to the shaft are assumed to be negligible. Also, the condition of the rotor is considered to be that of steady whirl, i.e. constant or slowly changing spin speeds, whirl speeds, and mode shapes.

These assumptions allow the whirl to be treated as simultaneous beam vibration of equal amplitude in the xy and xz planes, out of phase with each other by 90°. There is a jump condition in the beam vibration equations due to the disc at the mid-point.

4.2.2. Forces and Moments Acting on the Disc

The figure below shows the rotor under arbitrary planar deflection.
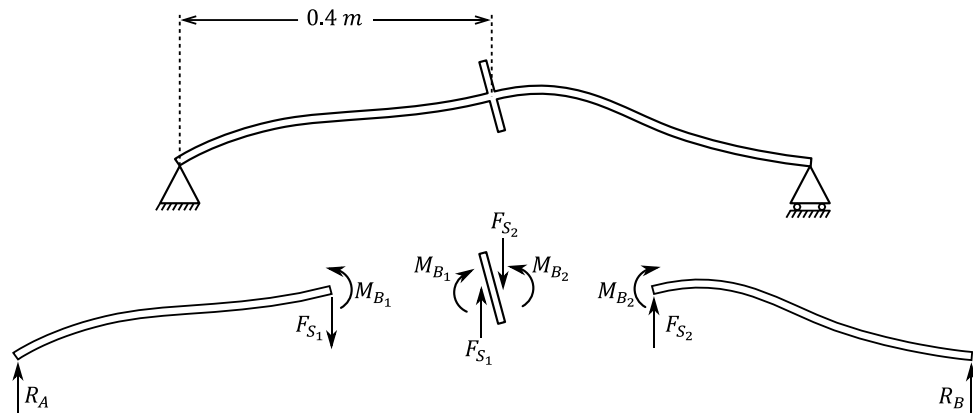
Figure 29: The deflected rotor, and free-body diagrams of the disc and of each half of the shaft

As seen in Figure 29, bending moments of magnitude M_{B_1} and M_{B_2} act on the left and right halves of the shaft at the points of interface with the disc. Equal and opposite moments act on the disc. The magnitude of the moment acting on each side of the disc is given by the flexural rigidity of the shaft times its curvature on that side.

Similarly, shear forces of magnitude F_{S_1} and F_{S_2} act on the shaft, and equal and opposite forces act on the disc. Their magnitudes are given by flexural rigidity times the x-rate of change of curvature.

The net force on the disc in the y direction is the sum of upward forces in the xy plane:

$$F_y = EIy'''(x)_{Left} - EIy'''(x)_{Right} \tag{68}$$

The net force on the disc in the z direction is the sum of upward forces in the xz plane:

$$F_z = EIz'''(x)_{Left} - EIz'''(x)_{Right} \tag{69}$$

The net moment on the disc in the z direction is the sum of counter-clockwise moments in the xy plane:

$$M_z = EIy''(x)_{Right} - EIy''(x)_{Left} \tag{70}$$

The net moment on the disc in the y direction is the sum of clockwise moments in the xz plane:

$$M_y = EIz''(x)_{Left} - EIz''(x)_{Right} \tag{71}$$

Since deflections are small, forces and moments in the x direction are small;

$$M_x = F_x = 0 \tag{72}$$

4.2.3. Orientation of the Disc

The orientation of the disc at any moment in time is described using three angles which are measured in the space-fixed coordinate system assumed. In the chosen order of transformation of orientation, these are $\omega_s t$, the angle about the x axis, θ_z, the tilt of the disc about the z axis, and θ_y, the tilt of the disc about the y axis.

The positive directions for $\omega_s t$, θ_z and θ_y are shown in Figure 30. Here, θ_z and θ_y are small, since they are the result of rotor deflection. $\omega_s t$ is not small, since it is the result of rotor spin.
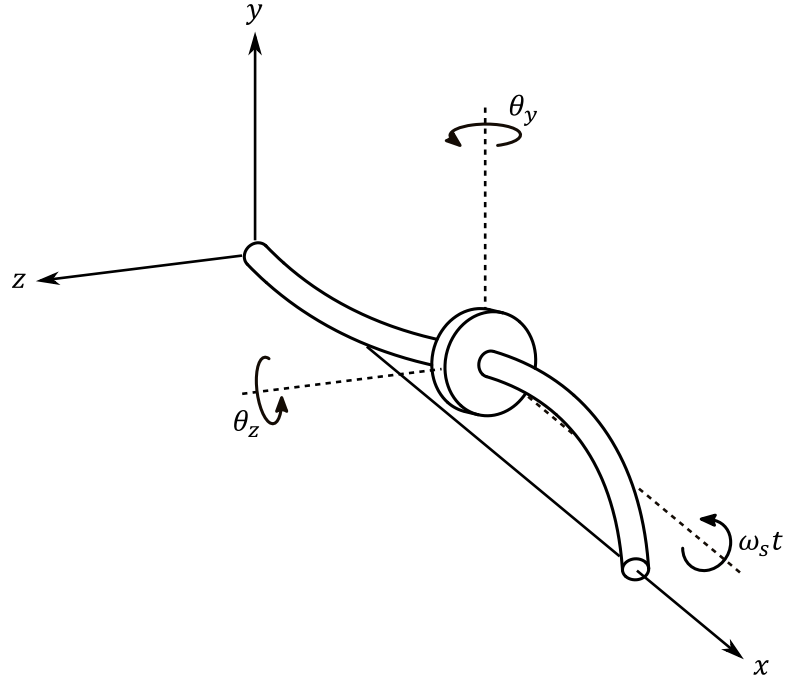
Figure 30: Positive directions for orientation angles of the central disc of the rotor

The rotation matrix corresponding to rotation by $\omega_s t$ about the x axis is:

$$R_1 = \begin{bmatrix} 1 & 0 & 0 \\ 0 & \cos \omega_s t & -\sin \omega_s t \\ 0 & \sin \omega_s t & \cos \omega_s t \end{bmatrix}$$

The rotation matrix corresponding to rotation by θ_z about the z axis is:

$$R_2 = \begin{bmatrix} \cos \theta_z & -\sin \theta_z & 0 \\ \sin \theta_z & \cos \theta_z & 0 \\ 0 & 0 & 1 \end{bmatrix}$$

The rotation matrix corresponding to rotation by θ_y about the y axis is:

$$R_3 = \begin{bmatrix} \cos \theta_y & 0 & \sin \theta_y \\ 0 & 1 & 0 \\ -\sin \theta_y & 0 & \cos \theta_y \end{bmatrix}$$

The rotation matrix, then, that transforms a vector embedded in the disc from its orientation in the rotor's undeflected state to its orientation in the deflected state is:

$$R = R_3 R_2 R_1$$

$$= \begin{bmatrix} \cos \theta_y & 0 & \sin \theta_y \\ 0 & 1 & 0 \\ -\sin \theta_y & 0 & \cos \theta_y \end{bmatrix} \begin{bmatrix} \cos \theta_z & -\sin \theta_z & 0 \\ \sin \theta_z & \cos \theta_z & 0 \\ 0 & 0 & 1 \end{bmatrix} \begin{bmatrix} 1 & 0 & 0 \\ 0 & \cos \omega_s t & -\sin \omega_s t \\ 0 & \sin \omega_s t & \cos \omega_s t \end{bmatrix}$$

48

$$R = \begin{bmatrix} \cos\theta_y \cos\theta_z & -\cos\theta_y \sin\theta_z \cos\omega_s t + \sin\theta_y \sin\omega_s t & \cos\theta_y \sin\theta_z \sin\omega_s t + \sin\theta_y \cos\omega_s t \\ \sin\theta_z & \cos\theta_z \cos\omega_s t & -\cos\theta_z \sin\omega_s t \\ -\sin\theta_y \cos\theta_z & \sin\theta_y \sin\theta_z \cos\omega_s t + \cos\theta_y \sin\omega_s t & -\sin\theta_y \sin\theta_z \sin\omega_s t + \cos\theta_y \cos\omega_s t \end{bmatrix}$$

$$(73)$$

4.2.4. Moment-of-Inertia Tensor of the Disc

When the rotor is undeformed, the axis of the disc lines up with the x axis. In this state, the moment-of-inertia tensor of the disc, expressed in the chosen space-fixed coordinate system, is

$$J_0 = \begin{bmatrix} J_{axial} & 0 & 0 \\ 0 & J_{transverse} & 0 \\ 0 & 0 & J_{transverse} \end{bmatrix} \tag{74}$$

and the moment of inertia of the disc in the deflected orientation can be found using the expression for tensor rotation:

$$J = R J_0 R^T \tag{75}$$

4.2.5. Angular Velocity of the Disc

The time rate of change any vector $\vec{n}$ of constant magnitude rotating with angular velocity $\vec{\omega}$ in a fixed reference frame is given by

$$\dot{\vec{n}} = \vec{\omega} \times \vec{n} \tag{76}$$

Now, if $\vec{n}$ is imagined to be embedded in the central disc of the rotor being considered, and if $\vec{n}_0$ is taken to be an arbitrary reference orientation corresponding to the undeflected state of the rotor, then

$$\vec{n} = R\vec{n}_0 \tag{77}$$

Since $\vec{n}_0$ is a constant reference orientation, differentiating with respect to time gives

$$\dot{\vec{n}} = \dot{R}\vec{n}_0 \tag{78}$$

Now, since R is a rotation matrix and therefore orthogonal,

$$RR^T = R^TR = I \tag{79}$$

Differentiating this with respect to time gives

$$R\dot{R}^T + \dot{R}R^T = 0$$

$$\dot{R}R^T = -R\dot{R}^T \tag{80}$$

Post-multiplying both sides by R,

$$\dot{R}R^TR = -R\dot{R}^TR$$

which, using (79), becomes

$$\dot{R} = -R\dot{R}^TR$$

Substituting this into (78) gives

$$\dot{\vec{n}} = -R\dot{R}^TR\vec{n}_0$$

which, using (77), becomes

$$\dot{\vec{n}} = -R\dot{R}^T\vec{n} \tag{81}$$

From (80), it is evident that $-R\dot{R}^T$ is skew-symmetric. Pre-multiplication by this matrix, then, is equivalent to the cross-product with its axial vector. This means that

$$\dot{\vec{n}} = \vec{p} \times \vec{n} \tag{82}$$

where $\vec{p}$ is given by

$$[p] = \begin{bmatrix} \left[-R\dot{R}^T\right]_{32} \\ \left[-R\dot{R}^T\right]_{13} \\ \left[-R\dot{R}^T\right]_{21} \end{bmatrix}$$

Comparing (82) with (76) makes it clear that $\vec{p} = \vec{\omega}$, and so

$$[\omega] = \begin{bmatrix} \left[-R\dot{R}^T\right]_{3\,2} \\ \left[-R\dot{R}^T\right]_{1\,3} \\ \left[-R\dot{R}^T\right]_{2\,1} \end{bmatrix} \tag{83}$$

Evaluating this using the expression for R from (73) gives

$$[\omega] = \begin{bmatrix} \sin\theta_y\,\dot{\theta}_z + \cos\theta_z\cos\theta_y\,\omega_s \\ \dot{\theta}_y + \sin\theta_z\,\omega_s \\ \cos\theta_y\,\dot{\theta}_z - \cos\theta_z\sin\theta_y\,\omega_s \end{bmatrix} \tag{84}$$

4.2.6. Angular Momentum of the Disc

Using J and ω from (75) and (83), the angular momentum can be found in terms of θ_y, θ_z, $\dot{\theta}_y$, $\dot{\theta}_z$, ω_s and t as

$$\vec{L} = J\vec{\omega} \tag{85}$$

4.2.7. Beam Vibration Equations

Based on the initial assumptions, the projections on the xy and xz planes of the profile of the beam are taken to be

$$y(x,t) = \begin{cases} W_1(x)\cos\omega_w t & 0m < x < 0.4m \\ W_2(x)\cos\omega_w t & 0.4m < x < 0.8m \end{cases} \tag{86}$$

and

$$z(x,t) = \begin{cases} W_1(x)\sin\omega_w t & 0m < x < 0.4m \\ W_2(x)\sin\omega_w t & 0.4m < x < 0.8m \end{cases} \tag{87}$$

for some deflected shape given by $W_1(x)$ and $W_2(x)$, and some whirl speed ω_w.

When ω_w is positive, displacement in the z direction lags displacement in the y direction by 90°. This means that the rotor passes through the $+z$ half of the xz plane 90° after passing through the $+y$ half of the xy plane.
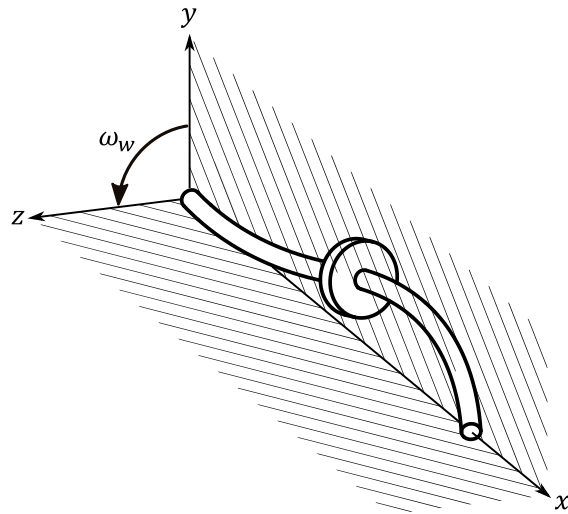
Figure 31: Assumed direction of whirl

ω_w is therefore in the positive x direction, i.e. in the same direction as ω_s. Positive values of ω_w, then, correspond to forward whirl. It follows that negative values of ω_w correspond to backward whirl.

The figure below shows an arbitrary deflected profile of the rotor in the xy plane. The observed mode shapes and frequencies of vibration would be the same in the xz plane.
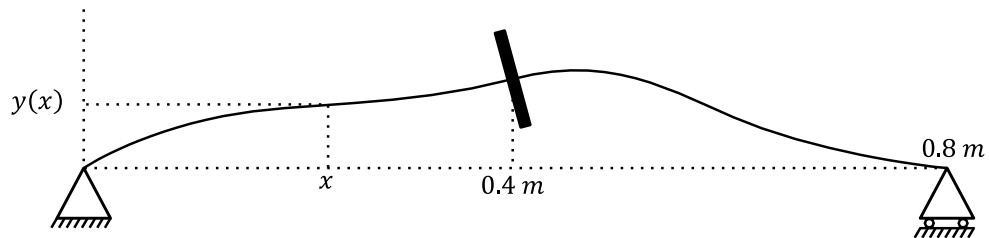
Figure 32: Deflected profile of the rotor in the xy plane

The beam obeys the differential equation

$$EIy'''' - \rho A\ddot{y} = 0 \tag{88}$$

between the left support and the disc, and again between the disc and the right support.

Based on the known form of solutions to (88), $W_1(x)$ and $W_2(x)$ are taken to be

$$W_1(x) = A_1 \sin \beta x + A_2 \cos \beta x + A_3 \sinh \beta x + A_4 \cosh \beta x \tag{89}$$

and

$$W_2(x) = A_5 \sin \beta x + A_6 \cos \beta x + A_7 \sinh \beta x + A_8 \cosh \beta x \tag{90}$$

where

$$\beta = \left(\frac{\rho A\omega_w^2}{EI}\right)^{\frac{1}{4}} \tag{91}$$

Immediately apparent boundary conditions include zero displacement and curvature at the simple supports, and continuity of displacement and slope at the disc i.e. at $x = 0.4$ (all values of x are understood to have units of meters).

$$W_1(0) = 0 \tag{92}$$

$$W_1''(0) = 0 \tag{93}$$

$$W_2(0.8) = 0 \tag{94}$$

$$W_2''(0.8) = 0 \tag{95}$$

$$W_1(0.4) = W_2(0.4) \tag{96}$$

$$W_1'(0.4) = W_2'(0.4) \tag{97}$$

The rate of change of angular velocity of the disc is equal to the net moment acting on it:

$$\vec{M} = \dot{\vec{L}}$$

Here, $\dot{\vec{L}}$ can be found by differentiating (85) with respect to time.

Using the expressions for the x, y and z components of the net moment acting on the disc from (70), (71), and (72), and using substitutions for $y(x)$ and $z(x)$ from (86) and (87) gives

$$EI \begin{bmatrix} 0 \\ \left(W_1''(0.4) - W_2''(0.4)\right)\sin \omega_w t \\ \left(W_2''(0.4) - W_1''(0.4)\right)\cos \omega_w t \end{bmatrix} = [\dot{L}] \tag{98}$$

Since deflections are small, the values of θ_z and θ_y can be taken to be equal to the slope of $y(x)$ and $z(x)$ at $x = 0.4$.

$$\theta_z = y'(0.4) = W_1'(0.4)\cos \omega_w t \tag{99}$$

$$\theta_y = -z'(0.4) = -W_1'(0.4)\sin \omega_w t \tag{100}$$

as seen in Figure 31, and

$$\dot{\theta}_z = -\omega_w W_1'(0.4)\sin \omega_w t \tag{101}$$

$$\dot{\theta}_y = -\omega_w W_1'(0.4)\cos \omega_w t \tag{102}$$

The net force acting on the disc is equal to its mass times its acceleration:

$$\vec{F} = m\vec{a}$$

Using the expressions for the x, y and z components of the net force acting on the disc from (68), (69), and (72), and using (86) and (87) gives

$$EI \begin{bmatrix} 0 \\ \left(W_1'''(0.4) - W_2'''(0.4)\right)\cos \omega_w t \\ \left(W_1'''(0.4) - W_2'''(0.4)\right)\sin \omega_w t \end{bmatrix} = m[a] \tag{103}$$

Now, the linear acceleration of the disc is equal to the linear acceleration of the shaft at $x = 0.4$, so, using (86) and (87), $[a]$ from (103) can be written as

$$[a] = \begin{bmatrix} 0 \\ \ddot{y}(0.4) \\ \ddot{z}(0.4) \end{bmatrix} = -\omega_w^2 \begin{bmatrix} 0 \\ W_1(0.4)\cos\omega_w t \\ W_1(0.4)\sin\omega_w t \end{bmatrix} \tag{104}$$

So,

$$EI \begin{bmatrix} 0 \\ (W_1'''(0.4) - W_2'''(0.4))\cos\omega_w t \\ (W_1'''(0.4) - W_2'''(0.4))\sin\omega_w t \end{bmatrix}$$
$$= -m\omega_w^2 \begin{bmatrix} 0 \\ W_1(0.4)\cos\omega_w t \\ W_1(0.4)\sin\omega_w t \end{bmatrix} \tag{105}$$

Now, since the equations governing the rotor should hold equally at every instant in time, $t = 0$ is arbitrarily chosen to be the moment of interest.

At $t = 0$, equations (98) and (105) give:

$$EI\big(W_2''(0.4) - W_1''(0.4)\big) = \dot{L}_{z\,(t=0)} \tag{106}$$

$$EI\big(W_1'''(0.4) - W_2'''(0.4)\big) = -m\omega_w^2 W_1(0.4) \tag{107}$$

At $t = 0$, equations (99) through (102) give:

$$\theta_z = W_1'(0.4) \tag{108}$$

$$\theta_y = 0 \tag{109}$$

$$\dot{\theta}_z = 0 \tag{110}$$

$$\dot{\theta}_y = -\omega_w W_1'(0.4) \tag{111}$$

4.2.8. Solution and Results

Equations (92) through (97), and (106) and (107) form a system of transcendental equations in ω_w with eight unknowns $A_1 .. A_8$ and one free parameter ω_s.

Substitutions (108) through (111) can be used to evaluate $\dot{L}_{y_{(t=0)}}$ for (106). However, since the expression arrived at contains nonlinear terms in $A_1 .. A_8$ due to the presence of sines and cosines of θ_z and θ_y in R (equation (73)) and therefore in J and ω, a truncated Taylor series expansion is used to linearize (106). All the other equations in the system are linear in $A_1 .. A_8$.

Figure 33 shows the determinant of the coefficient matrix of the system of equations now assembled, plotted against ω_w for three different values of ω_s. Since the value of this determinant varies over a very large range, the vertical axis is mapped to the logarithm of its magnitude for better scaling.

$$\omega_s = 0 \; rad/s$$

$$\omega_s = 5000 \; rad/s$$

$$\omega_s = 10000 \; rad/s$$
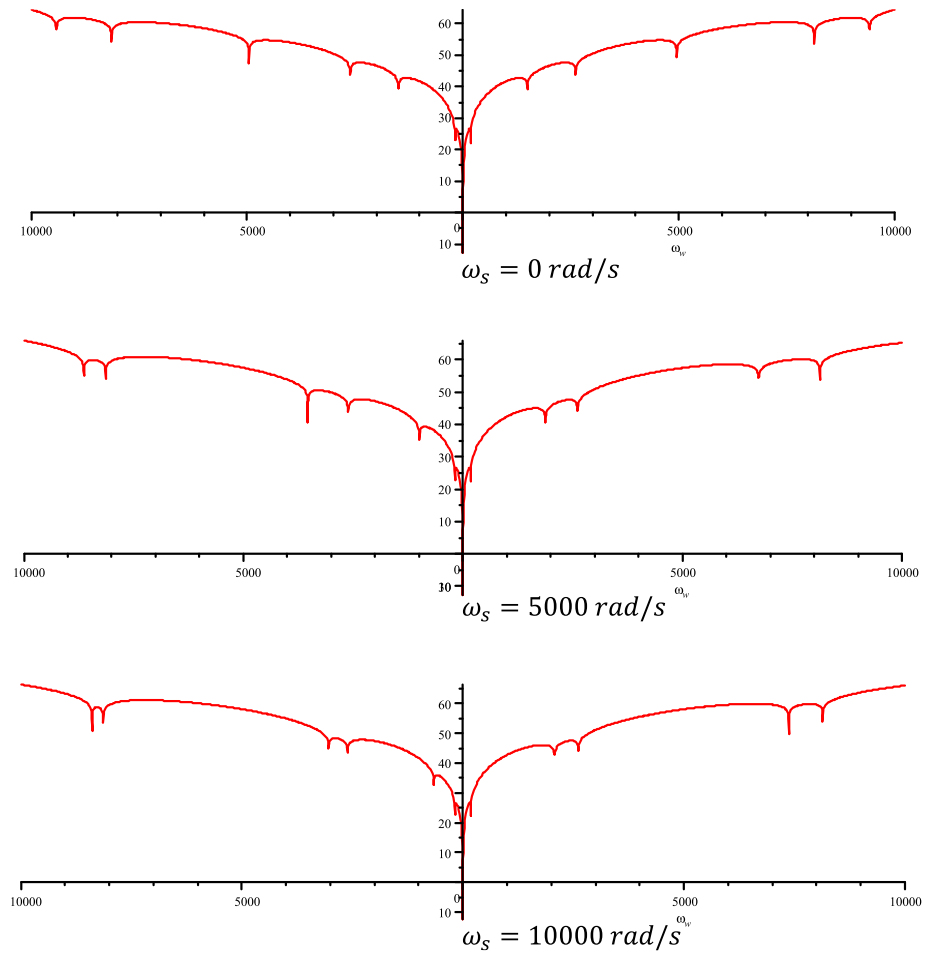
Figure 33: Log of determinant of coefficient matrix plotted against whirl speed for three values of spin speed

56

Each asymptotic dip in the graph corresponds to a zero-crossing of the determinant, and therefore an eigenvalue of the system and a natural frequency of the rotor. The left half of the graph corresponds to backward whirl and the right half corresponds to forward whirl. At zero spin speed, as expected, the natural frequencies are symmetrically distributed about the vertical axis. These are the pure bending vibration frequencies of the rotor. As the spin speed increases, backward whirl frequencies move towards zero and forward whirl frequencies move away from zero. It may also be noted that the first, third, and fifth natural frequencies on either side of zero do not change significantly as the spin speed is changed.

4.3. Campbell Diagram

Plotting of a Campbell diagram from the expression for the determinant as found involves iterating through values of ω_w with ω_s held fixed, and evaluating the expression at each point to check for zero-crossings in the range of interest. Repeating this process for different values of ω_s yields a set of (ω_s, ω_w) points which can be plotted and interpolated between. The resultant plot is shown below.
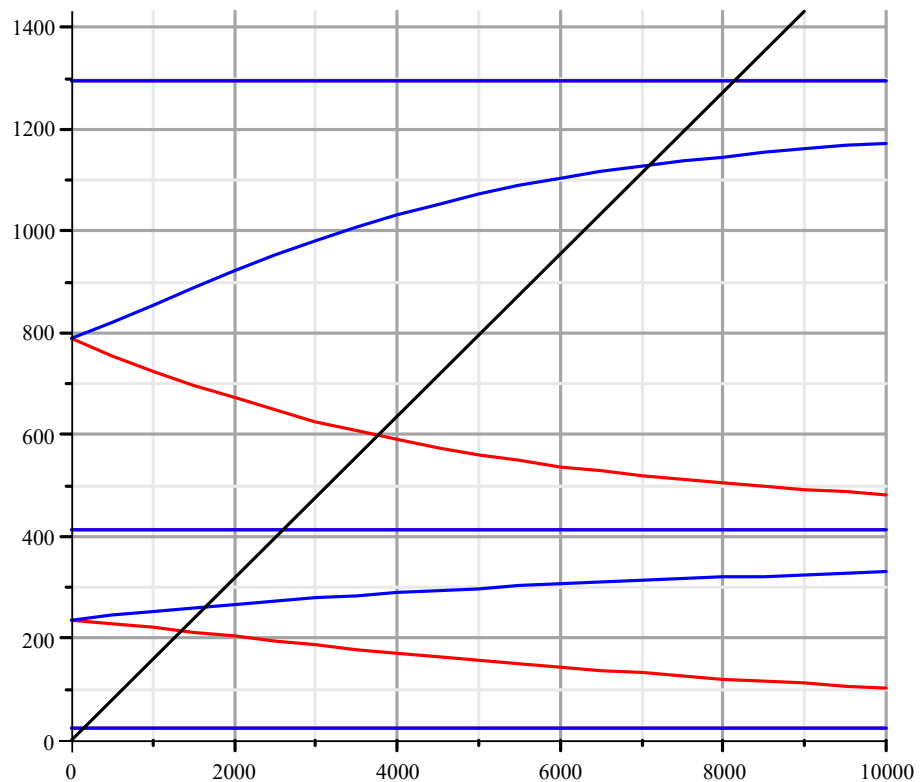
Figure 34: Natural frequency (Hertz) against spin speed (rad/s)

Here, the natural frequency of the rotor is on the vertical axis and its spin speed is on the horizontal axis. The blue lines represent forward whirl and the red lines represent backward whirl only. The black line has slope 1 and points at which it crosses the red and blue lines indicate critical speeds.

4.4. Ansys Results

The Campbell diagram obtained from ANSYS simulation (5-point analysis) is shown below:
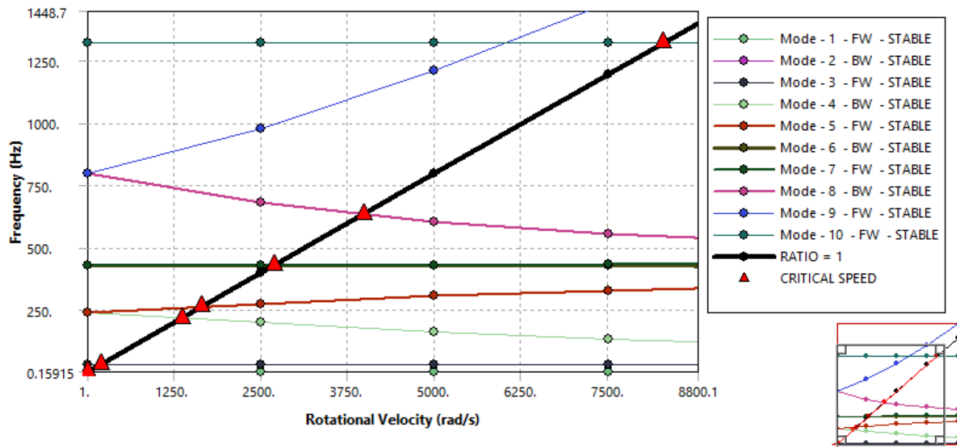
Figure 35: Campbell diagram generated by ANSYS

Figure 35 is, qualitatively, a good match with the Campbell diagram generated from the beam vibration equations (Figure 34), except for the forward whirl branch of the fourth vibrational mode. The slope seen in Figure 34 of the line corresponding to the fourth forward whirl mode is shallower, due to which an additional critical speed is predicted which does not appear in the ANSYS results.

The differences between the ANSYS results and the predictions based on beam vibration equations are presumed to be due largely to gyroscopic effects of the shaft. As the radius of the disc is increased, the ratio of the mass moments of inertia about the rotor axis of the disc and the shaft will increase rapidly. This is expected to improve the match between results obtained from the two methods.

5. THE SEMI-ANALYTICAL ROTOR MODEL

All approaches to rotor whirl prediction discussed thus far have been fully analytical, i.e. they have been developed from first principles using various simplifying assumptions about each rotor. Such an approach, however, is often not practical or helpful while studying more realistic rotors, such as the sCO_2 rotor that has motivated this work. In the following, a novel semi-analytical method is presented, which, it is hoped, may to some extent bridge the gap between reliable but relatively opaque FEM simulations and more transparent but generally impractical fully analytical formulations.

5.1. Overview of the Lagrangian Formulation

Unlike the formulation in Section 4, which takes a Newtonian approach to analysis through momentum balance equations, the method now presented will use a Lagrangian approach. Expressions will first be derived for the total kinetic and potential energies of the system in terms of a basis of generalized coordinates constructed to be well-suited to the rotor system at hand. Approximate equations of motion for the system will then be obtained by constructing the Lagrangian and writing Lagrange's equations. Finally, finding eigenvalues of this system of equations for several different values of imposed spin speed on the system will allow the change in natural frequencies with respect to spin speed, i.e., the Campbell diagram, to be plotted.

5.2. Method and Analysis

The method used here involves:

1. Modelling the rotor by describing its inertial and elastic characteristics as functions of a spatial coordinate (here, x) along the nominal rotor axis,

2. Expressing the kinetic and potential energy of the rotor in terms of the state of the rotor at time t and the rotor spin speed ω_s,

3. Generating orthogonal bases of assumed modes and substituting them into the energy expressions obtained, and finally

4. Writing Lagrange's equations for the reduced rotor and finding eigenvalues of the system at different values of ω_s to obtain expected natural frequencies.

5.2.1. Assumptions and Modelling

The scope of this work includes rotors that can be treated as axisymmetric, undamped, and supported with or without overhangs on short bearings. The focus is on lateral or bending vibration, and twisting of the shaft is not taken into account.

5.2.1.1. Coordinate System

A fixed coordinate system is considered whose x-axis lies along the nominal or undeformed spin axis of the rotor, as seen in Figure 36. One end of the rotor is at $x = 0$, and its supports are located at $x = s_1$ and $x = s_2$. The length of the rotor is l.
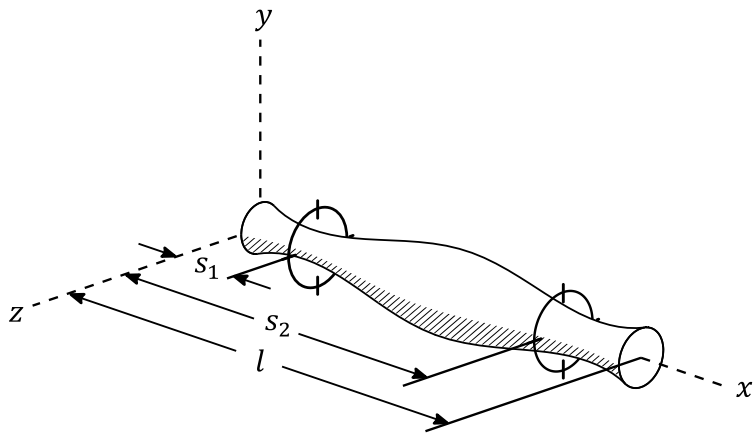
Figure 36: Fixed coordinate system with x-axis along rotor

5.2.1.2. Degrees of Freedom

In a Timoshenko beam, shear angle and lateral deflection can, in theory, change independently of each other; they therefore form separate degrees of freedom. For the rotor, deflection both in the xy and xz planes must be considered, and so the system has four degrees of freedom corresponding to each point along its length:

$y(x, t)$, the deflection along the y-axis,

$z(x, t)$, the deflection along the z-axis,

$\phi_y(x, t)$, the shear angle about the y-axis, and

$\phi_z(x, t)$, the shear angle about the z-axis.

The rotor spin speed ω_s, and by extension the spin angle $\omega_s t$ at any time t, are considered to be externally imposed and are therefore input parameters to the system.

5.2.1.3. Rotor Characteristics

The rotor is modelled using four functions of x. These are:

$\rho A(x)$, the linear mass density,

$J_a(x)$, the axial mass moment of inertia per unit length,

$EI(x)$, the flexural rigidity, and

$KAG(x)$, the effective shear rigidity.

There are several approaches imaginable to obtaining expressions for these functions. This paper contains demonstrations both of using theory to calculate them directly and of fitting curves to data obtained from simulations. It is also conceivable that curves might be fit for this purpose to experimental data.

5.2.2. Potential Energy

When shear is not considered (i.e., in Euler-Bernoulli beam theory), the strain energy per unit length at a point along a beam is given by half times the flexural rigidity of the beam times its curvature squared. Shearing of the beam adds to its slope, so this contribution may be removed while calculating the bending part of the potential energy, resulting in the expression

$$PE_b(x,t) = \frac{1}{2} EI \left((y' - \phi_z)'^2 + \left(-z' - \phi_y \right)'^2 \right) \tag{112}$$

for the potential or strain energy per unit length due to bending in both planes.

The strain energy per unit length due to shearing is given by

$$PE_s(x,t) = \frac{1}{2} KAG \left(\phi_y^2 + \phi_z^2 \right). \tag{113}$$

For a rotor on rigid bearings, the total potential energy of the system is the sum of PE_b and PE_s, integrated over the length of the rotor:

$$V_{RB} = \int_o^l (PE_b + PE_s)dx. \tag{114}$$

If there is a simple compliance in the bearings, i.e. a known radial bearing stiffness, then the total potential energy additionally includes the energy stored in the bearings:

$$V_{CB} = \int_0^l (PE_b + PE_s)dx + \frac{1}{2}k_{s1}(y(s_1,t)^2 + z(s_1,t)^2) \\ + \frac{1}{2}k_{s2}(y(s_2,t)^2 + z(s_2,t)^2) \tag{115}$$

where k_{s1} and k_{s2} are the stiffnesses of the bearings at s_1 and s_2.

5.2.3. Translational Kinetic Energy

Each infinitesimal element along the length of the rotor has kinetic energy due to the element's rotation about its center of mass, as well as due to translation of its center of mass. Since the rotor is assumed to be axisymmetric, the elements are thin discs, and their centers of mass lie on the rotor mid-line.

The kinetic energy due to translation is simply half times the disc's mass times its velocity squared, so the kinetic energy due to translation per unit length is

$$KE_t(x,t) = \frac{1}{2}\rho A(\dot{y}^2 + \dot{z}^2). \tag{116}$$

5.2.4. Rotational Kinetic Energy

The rotational kinetic energy per unit length of the rotor would be given by

$$KE_r(x,t) = \frac{1}{2}(\vec{\Omega}.J\vec{\Omega}) \tag{117}$$

where Jdx is the moment of inertia tensor of a rotor element of length dx as seen from the fixed reference frame while the rotor is spinning and deformed, and $\vec{\Omega}$ is its angular velocity. The first step to finding expressions for J and $\vec{\Omega}$ is to define the orientation of the disc as a function of time.

It should be noted that unlike in Section 4, where the rotor was treated as a discrete disc on a shaft and J was its moment-of-inertia tensor, the current treatment is

for a continuous rotor and J here is the length-normalized moment-of-inertia tensor, i.e., the moment-of-inertia tensor of a rotor element divided by its length.

5.2.5. Orientation of the Rotor Element

Each infinitesimal disc along the rotor is assumed to be transformed from its orientation in the rotor's stationary and undeformed state to that in the spinning and deformed state through three rotations, in an order consistent with the findings of Choi et al. [3]. The rotations are shown in Figure 37. First, the disc is rotated by θ_z about the z-axis, then by θ_y about the once-rotated y-axis, and finally by $\omega_s t$ about the twice-rotated x-axis.
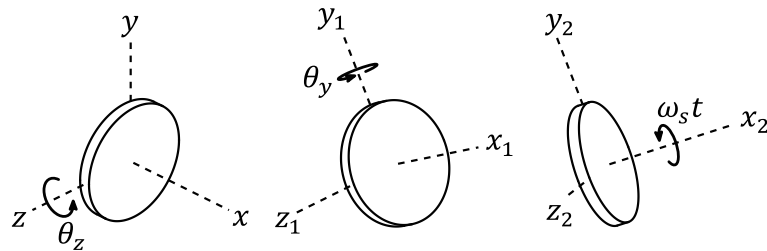
Figure 37: (In order, left to right) rotations defining orientation of rotor element

Rotation matrices R_1, R_2, and R_3 corresponding to the rotations shown in Figure 37 (i.e., rotation matrices that will rotate a vector embedded in the disc through the angles described) can be obtained using the general formula for a rotation matrix to rotate a vector through θ about $\hat{n}$,

$$R(\hat{n}, \theta) = (\cos \theta)I + (1 - \cos \theta)[\hat{n}][\hat{n}]^T + (\sin \theta)S(\hat{n}) \tag{118}$$

where I is the 3×3 identity matrix and $S(\hat{n})$ is the skew-symmetric matrix corresponding to a cross-product with $\hat{n}$.

Equivalently, R_1, R_2 and R_3 can be obtained using known basic rotations as follows:

$$R_1 = \begin{bmatrix} \cos \theta_z & -\sin \theta_z & 0 \\ \sin \theta_z & \cos \theta_z & 0 \\ 0 & 0 & 1 \end{bmatrix} \tag{119}$$

$$R_2 = R_1 \begin{bmatrix} \cos \theta_y & 0 & \sin \theta_y \\ 0 & 1 & 0 \\ -\sin \theta_y & 0 & \cos \theta_y \end{bmatrix} R_1^T \tag{120}$$

$$R_3 = R_2 R_1 \begin{bmatrix} 1 & 0 & 0 \\ 0 & \cos \omega_s t & -\sin \omega_s t \\ 0 & \sin \omega_s t & \cos \omega_s t \end{bmatrix} (R_2 R_1)^T \qquad (121)$$

Now, the net rotation matrix is given by

$$R = R_3 R_2 R_1, \qquad (122)$$

which is a function of x and t.

5.2.6. Angular Velocity

Since R describes the orientation of every rotor element as a function of time, an expression for the angular velocity can be derived from it, as seen in Section 4.2.5; $[\Omega]$ is found to be the axial vector of $-R\dot{R}^T$, i.e.

$$[\Omega] = \begin{bmatrix} -R\dot{R}^T {}_{3,2} \\ -R\dot{R}^T {}_{1,3} \\ -R\dot{R}^T {}_{2,1} \end{bmatrix}. \qquad (123)$$

This evaluates to

$$[\Omega] = \begin{bmatrix} -\dot{\theta}_y \sin \theta_z + \omega_s \cos \theta_z \cos \theta_y \\ \dot{\theta}_y \cos \theta_z + \omega_s \sin \theta_z \cos \theta_y \\ \dot{\theta}_z - \omega_s \sin \theta_y \end{bmatrix}. \qquad (124)$$

It may be noted that the same expression can be arrived at through

$$\vec{\Omega} = \dot{\theta}_z \hat{z} + \dot{\theta}_y R_1 \hat{y} + \omega_s R_2 R_1 \hat{x} \qquad (125)$$

where $\hat{x}$, $\hat{y}$ and $\hat{z}$ are unit vectors along the x, y and z axes.

5.2.7. Moment of Inertia Tensor of the Rotor Element

Since the rotor element is a disc and is infinitesimally thin, its transverse mass moments of inertia are equal to each other and to half of its axial mass moment of inertia. The moment of inertia tensor of the disc in its undeformed state, therefore, is $J_0 dx$, where

$$J_0 = \begin{bmatrix} J_a & 0 & 0 \\ 0 & \dfrac{J_a}{2} & 0 \\ 0 & 0 & \dfrac{J_a}{2} \end{bmatrix} \tag{126}$$

In the deformed state, this tensor is transformed by R, so

$$J = RJ_0R^T. \tag{127}$$

5.2.8. Algebraic Approximation to Rotational Kinetic Energy

Substituting the expressions for $\vec{\Omega}$ and J from (124) and (127) into (117) results in an expression for rotational kinetic energy per unit length that contains trigonometric functions of θ_z, θ_y, and $\omega_s t$. A Taylor expansion up to quadratic terms about θ_z and θ_y is used to approximate this transcendental expression, so that the system formed after the once-differentiation of energy in Lagrange's equations may be linear.

θ_z and θ_y describe the inclination of the spin axis of the rotor element. Since Timoshenko theory considers plane sections to remain plane, it is appropriate to think of the shearing of the beam as relative sliding between successive infinitesimal discs, as seen in Figure 38. This makes it clear that the inclination of the spin axis is given by the inclination of the mid-line minus the shear angle.
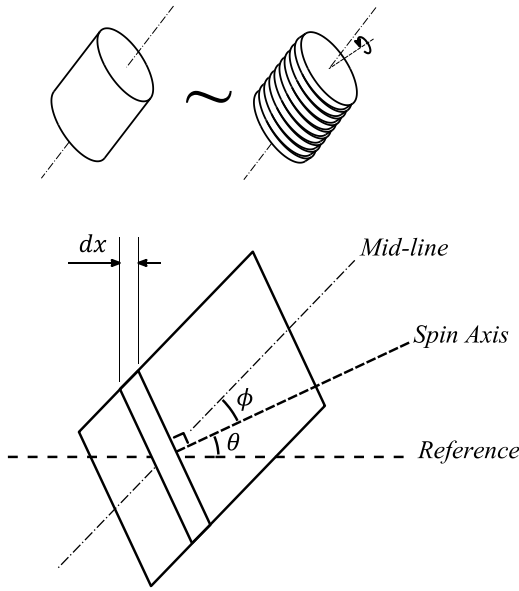
Figure 38: Shear angle and the inclination of the spin axis

$y' - \phi_z$ can now be substituted for θ_z, and $-z' - \phi_y$ for θ_y, into the algebraic expression obtained earlier. $\omega_s t$ and trigonometric functions of it must be retained since $\omega_s t$ is not small; this is acceptable since ω_s is a prescribed system parameter for which a numerical value can be used.

5.2.9. Total Kinetic Energy

Having obtained expressions for the kinetic energies per unit length of the rotor due to translation and due to rotation, the total kinetic energy of the system can be found as

$$T = \int_0^l (KE_t + KE_r)dx \tag{128}$$

using KE_t from (116) and the approximation to KE_r obtained as described in Section 5.2.8.

5.2.10. Assumed Modes

The expressions thus far obtained for the total kinetic and potential energies of the system are for a continuous or infinite-degree-of-freedom system. Hamilton's principle can be used to obtain, from these, PDEs governing the vibration of the rotor. However, the PDE solution can be bypassed by directly inserting a finite dimensional approximation into the Lagrangian. This is called the method of assumed modes.

66

Polynomials and sinusoids are common choices for assumed mode shapes in beam vibration problems, including for rotor whirl. Of these, sinusoids' inherent periodicity makes them best suited for end-supported systems, whereas polynomials are preferable when the system has overhangs. The disadvantage of the standard polynomial basis, however, is that it is not orthogonal. Non-orthogonal bases are, in general, less reliable than orthogonal bases and render computations more prone to truncation error and other numerical artefacts. As such it is sensible to construct and use an orthogonal basis of polynomial assumed mode shapes that is suitable to the system under consideration.

If on rigid bearings, a rotor's lateral displacement is constrained to zero at the support locations. The polynomials

$$U_k(x) = x^{k-1}(x - s_1)(x - s_2) \ , \ \ k \in \{1, 2, \cdots, n\} \tag{129}$$

are therefore considered, which have forced roots at s_1 and s_2. Figure 39 shows an example of such a basis of five polynomials with $l = 1$, $s_1 = 0.2$ and $s_2 = 0.8$.
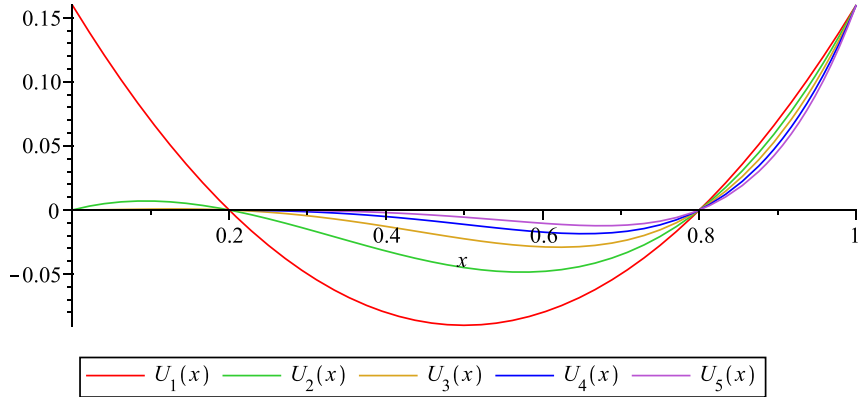
Figure 39: Non-orthogonal polynomial basis with forced roots

From here, the Gram-Schmidt process can be used to construct a set of polynomials $W_1(x) \cdots W_n(x)$ that are orthogonal in $x \in [0, l]$. $W_k(x)$ would be given by

$$W_k(x) = U_k(x) - \sum_{i=1}^{k-1} \frac{W_i(x) \int_0^l W_i(x) U_k(x) dx}{\int_0^l W_i(x)^2 dx} \tag{130}$$

or by a similar expression with suitable normalization. Figure 40 shows an example of such an orthogonalized polynomial basis with forced roots.
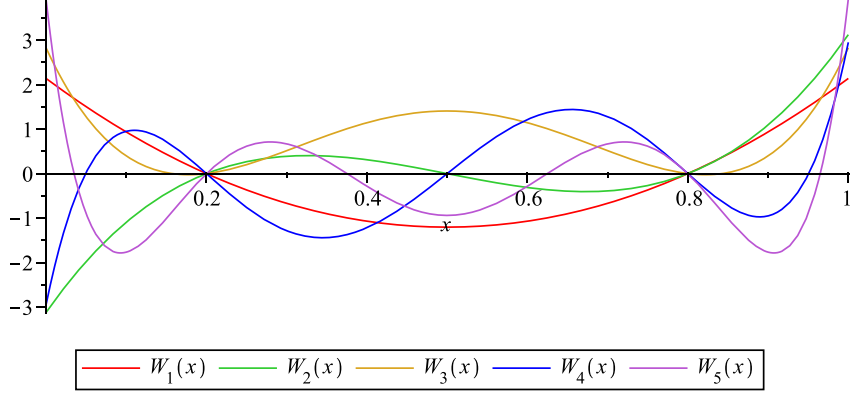
**Figure 40: Orthogonalized basis of polynomials with forced roots**

$W_1(x) \cdots W_n(x)$ clearly retain zeroes at $x = s_1$ and $x = s_2$. Therefore, their use in assumed modes for deflection of a rotor on rigid bearings circumvents the need for explicit boundary conditions.

Shear in the beam is not subject to any hard constraints such as those on deflection at the supports, so a more general orthogonal basis $P_1(x) \cdots P_n(x)$ similar to Legendre's polynomials is used. A simple polynomial basis $H_1(x) \cdots H_n(x)$ is first constructed:

$$H_k(x) = x^{k-1} \tag{131}$$

Figure 41 shows $H_1(x) \cdots H_5(x)$ for $l = 1$.
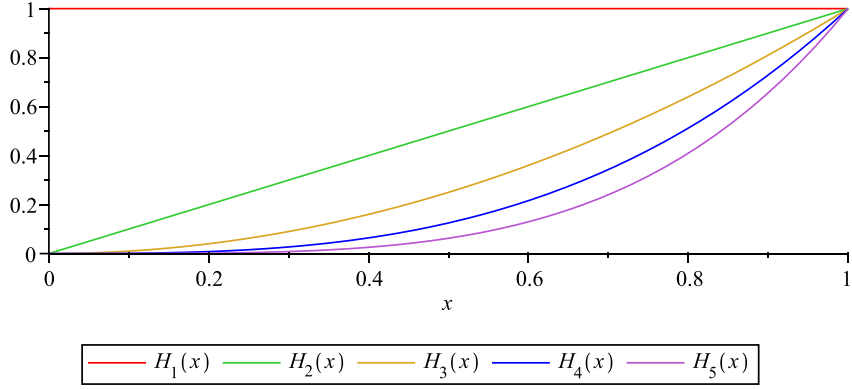

Figure 41: Simple polynomial basis

This basis is then orthogonalized:

$$P_k(x) = H_k(x) - \sum_{i=1}^{k-1} \frac{P_i(x) \int_0^l P_i(x) H_k(x) dx}{\int_0^l P_i(x)^2 dx} \tag{132}$$

68

Figure 42 shows an example of an orthogonalized polynomial basis without forced roots.
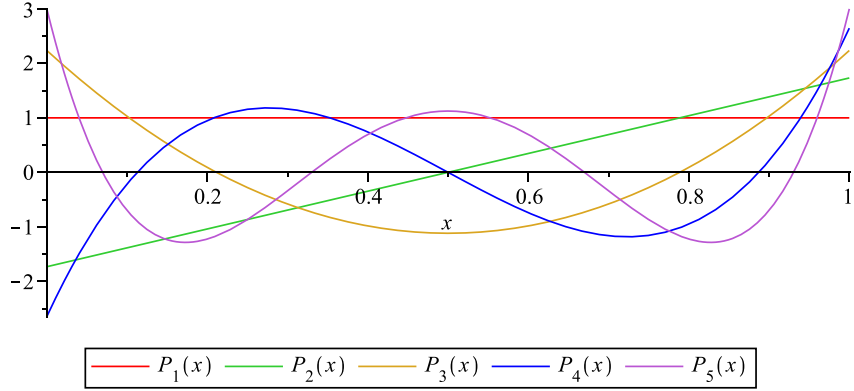

Figure 42: Orthogonalized polynomial basis without forced roots

If on compliant bearings, a rotor's displacement is generally nonzero at the support locations, so it is sensible for $W_1(x) \cdots W_n(x)$ to be constructed identically to $P_1(x) \cdots P_n(x)$ from (131) and (132). It may be noted that in moving to this more general basis, the highest order of assumed-mode shape for deflection is reduced by 2. The total number of assumed-mode shapes must therefore be increased by 2 in order to maintain the accuracy of results.

After the construction of appropriate assumed-mode bases, the deflection and shear in the beam are written as

$$y(x,t) = \sum_{k=1}^{n} W_k(x) q_k(t) \tag{133}$$

$$z(x,t) = \sum_{k=1}^{n} W_k(x) q_{k+n}(t) \tag{134}$$

$$\phi_y(x,t) = \sum_{k=1}^{n} P_k(x) q_{k+2n}(t) \tag{135}$$

69

$$\phi_z(x,t) = \sum_{k=1}^{n} P_k(x)q_{k+3n}(t) \tag{136}$$

where n is the number of assumed mode shapes each for deflection and shear and $q_1(t) \cdots q_{4n}(t)$ are the generalized coordinates for the MDOF system formed.

5.2.11. Finding Natural Frequencies

The Lagrangian for the system,

$$L = T - V \tag{137}$$

can be computed using the expression for total kinetic energy obtained as described in Section 5.2.9 and with V equal either to V_{RB} from (114) or to V_{CB} from (115) depending on whether the bearings are rigid or compliant. The assumed modes can then be inserted by substituting the expressions for y, z, ϕ_y and ϕ_z from (133) through (136) into L.

Now, writing Lagrange's equations

$$\frac{d}{dt}\frac{\partial L}{\partial \dot{q}_k} - \frac{\partial L}{\partial q_k} = 0 \ , \ \ k \in \{1, 2, \cdots, 4n\} \tag{138}$$

results in a system of the form

$$M[\ddot{q}] + G[\dot{q}] + K[q] = 0 \tag{139}$$

where M, G, and K are $4n \times 4n$ matrices. The eigenvalues of this system can be found through reduction to a generalized eigenvalue problem by stacking matrices to form an $8n \times 8n$ system, as follows:

$$\begin{bmatrix} M & G \\ [0] & I \end{bmatrix} \begin{bmatrix} [\ddot{q}] \\ [\dot{q}] \end{bmatrix} + \begin{bmatrix} [0] & K \\ -I & [0] \end{bmatrix} \begin{bmatrix} [\dot{q}] \\ [q] \end{bmatrix} = 0 \tag{140}$$

The natural frequencies of the rotor are given by the imaginary parts of the eigenvalues of (140). A Campbell diagram can be obtained by plotting the change in the absolute values of these imaginary parts as different numerical values of ω_s are used.
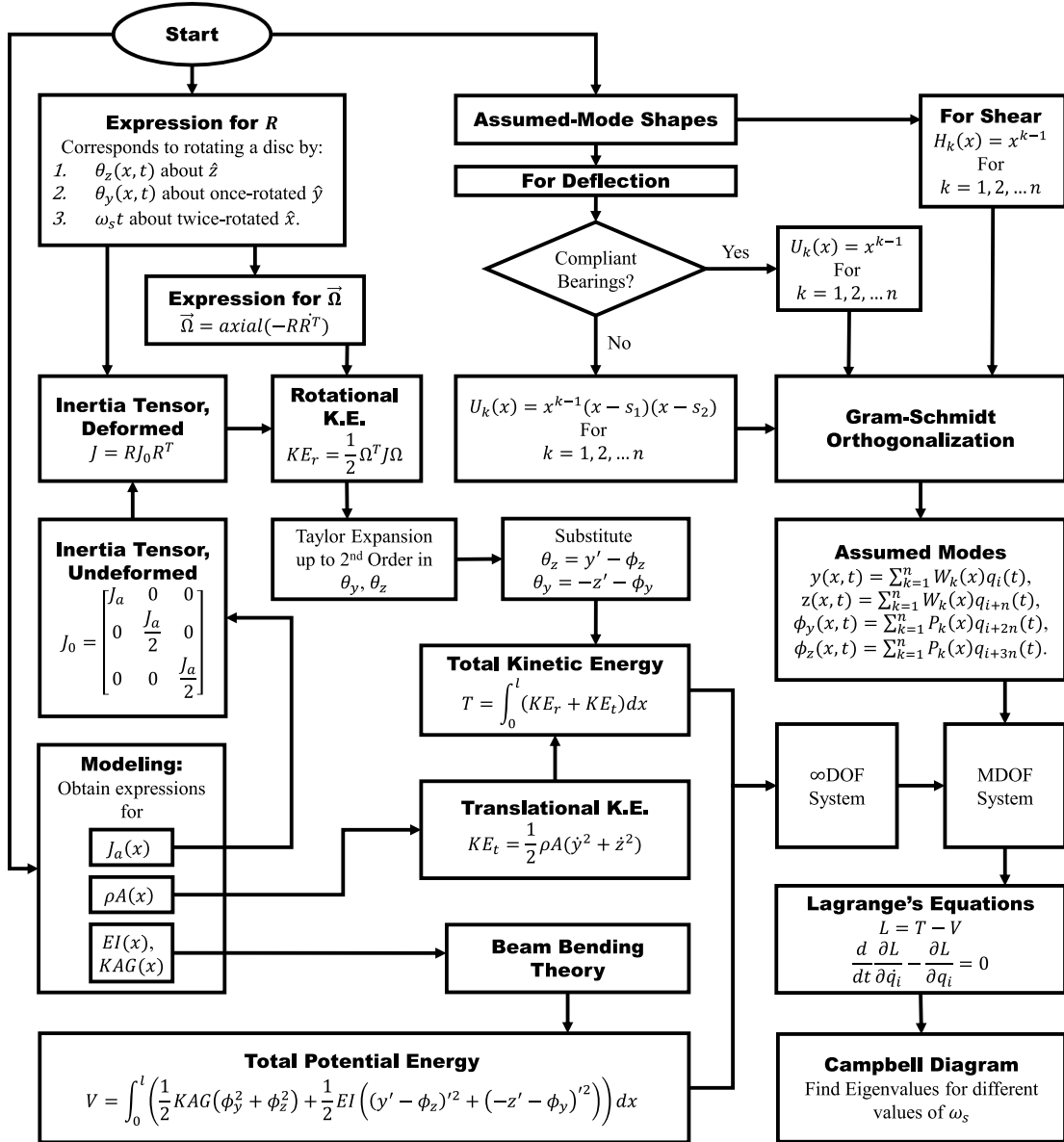

Figure 43: Semi-analytical whirl prediction method overview

5.3. Test Case 1: Tapered Hollow Rotor

The first rotor considered for validation is conical and has a conical hole running through it, as shown in Figure 44.
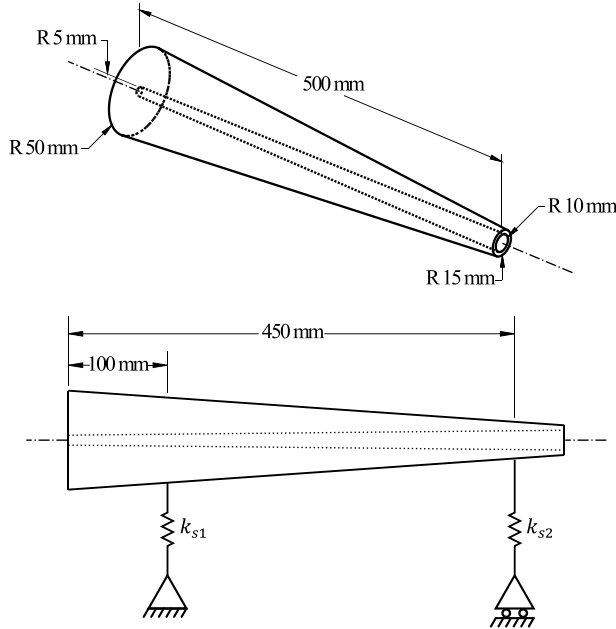

Figure 44: Tapered hollow rotor

The rotor is assumed to be made of steel with a density of 7850 Kg/m^3, Young's modulus equal to 2×10^{11} Pa and shear modulus of 7.69×10^{10} Pa.

Since the inner and outer radii of this rotor vary simply as linear functions of x, the characteristics of the rotor can easily be calculated using formulae for annular sections:

$$\rho A(x) = 7850 \text{ Kg/m}^3 \times \pi(r_o(x)^2 - r_i(x)^2) \tag{141}$$

$$J_a(x) = \frac{1}{2} \times \rho A(x) \times (r_o(x)^2 + r_i(x)^2) \tag{142}$$
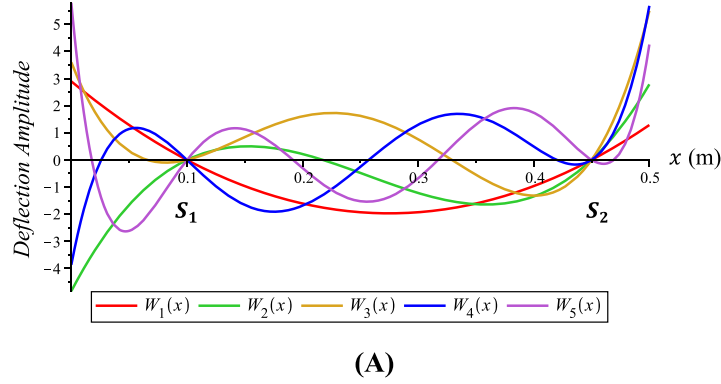
$$EI(x) = 2 \times 10^{11} \text{ Pa} \times \frac{\pi}{4} \times (r_o(x)^4 - r_i(x)^4) \tag{143}$$

$$KAG(x) = 0.892 \times \pi(r_o(x)^2 - r_i(x)^2) \times 7.69 \times 10^{10} \text{ Pa} \tag{144}$$
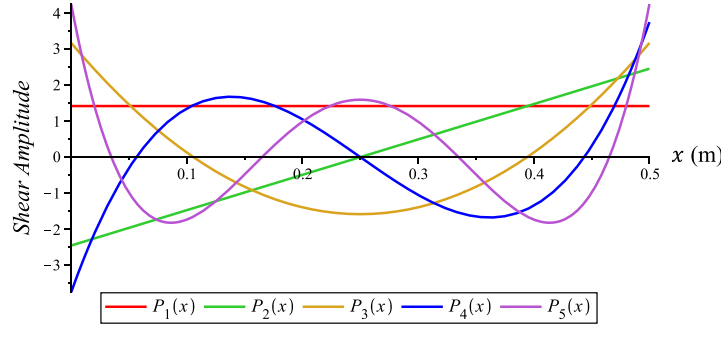
where $r_i(x)$ and $r_o(x)$ are, respectively, the internal and external radii of the rotor at x.

72

Here, the value of 0.892 for the shear factor is arrived at by averaging, over the range of internal and external radii of the rotor, the results of a formula by Hutchinson [16] for the shear factor of annular sections.

The rotor is first considered on rigid bearings (infinite bearing stiffnesses). Five assumed-mode shapes are used, and as described in Section 5.2.10, $W_1(x) \cdots W_5(x)$ are constructed with forced roots at $s_1 = 0.1$ and $s_2 = 0.45$. Plots of the assumed mode shapes used are shown in Figure 45.

(A)

**(B)**

Figure 45: Assumed mode shapes with rigid bearings: (A) For deflection and (B) For shear of the tapered hollow rotor

The tapered hollow rotor is also considered on compliant bearings of different stiffnesses, with seven assumed-mode shapes for shear and the same seven for deflection.

Natural frequency predictions are compared in Section 5.6.1 with output from simulations in Ansys.

5.4. Test Case 2: Multi-Stepped Rotor

The next test case is the rigidly supported multi-stepped rotor shown in Figure 46. Formulae like those used in Section 5.3 are used to find the linear mass density, axial mass moment of inertia per unit length, flexural rigidity, and shear rigidity at 20 equally spaced points along the rotor. 17th degree polynomials are then fit to this data, allowing for some smoothing of slope and curvature. Here again, values representative of steel are used for material properties.
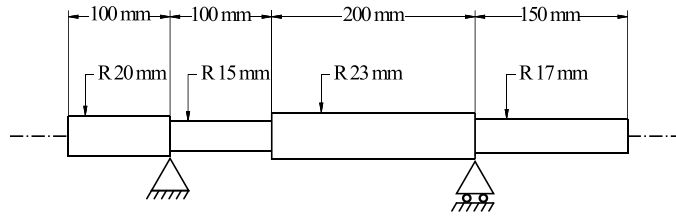

Figure 46: Multi-stepped rotor

Plots of the obtained polynomial approximations to $\rho A(x), J_a(x), EI(x)$ and $KAG(x)$ are shown in Figure 47.
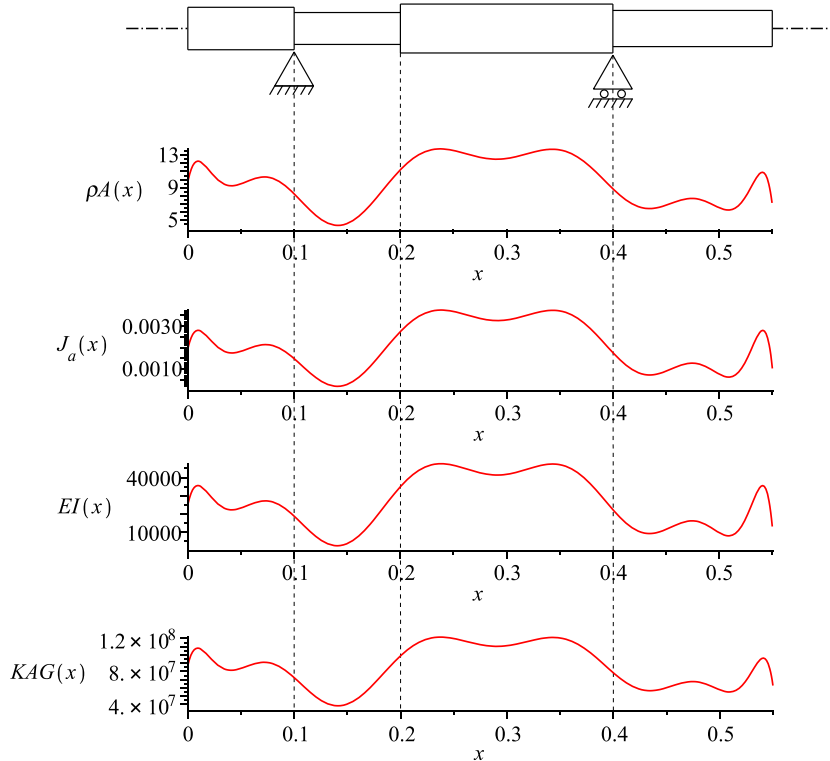

Figure 47: Polynomials fit to characteristics of multi-stepped rotor

A Campbell diagram generated using these polynomials, and another generated using direct piecewise application of formulae, using ten assumed mode shapes in each case, are compared in Section 5.6.2.

5.5. The sCO$_2$ Rotor

A version of the sCO$_2$ rotor design is shown in Figure 48, stripped down to its essential components from a rotordynamic standpoint. Two discs at either end simulate the mass and inertia of impellers, and the laminated core is replaced with a solid piece for which Young's modulus is assumed to be approximately 0.8×10^9 Pa and the shear modulus 0.3×10^9 Pa, based on the findings of Garvey [14] and Garvey et al. [15]. A representative value of 1.5×10^8 N/m is assumed for the bearing stiffnesses k_{s1} and k_{s2}.
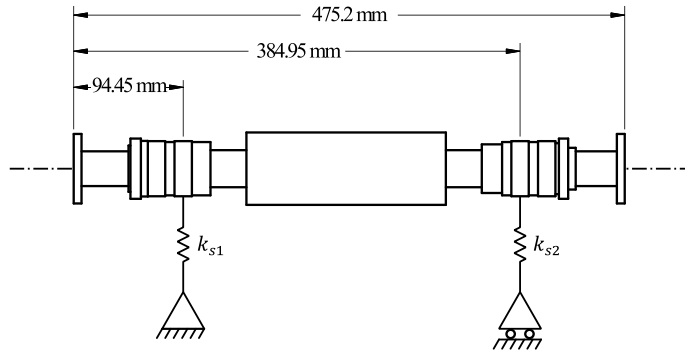
Figure 48: The simplified sCO$_2$ rotor

The CAD geometry for this rotor is divided into eight pieces as seen in Figure 49. The average linear mass density and axial mass moment of inertia per unit length in each of these pieces is calculated by dividing its mass and x-axis inertia readouts by its length. These values mapped to the locations of the mid-points of the eight rotor pieces, plus the first and last of these values duplicated at the ends of the rotor, form a dataset to which 6$^\text{th}$ degree polynomials are fit to serve as expressions for $\rho A(x)$ and $J_a(x)$.
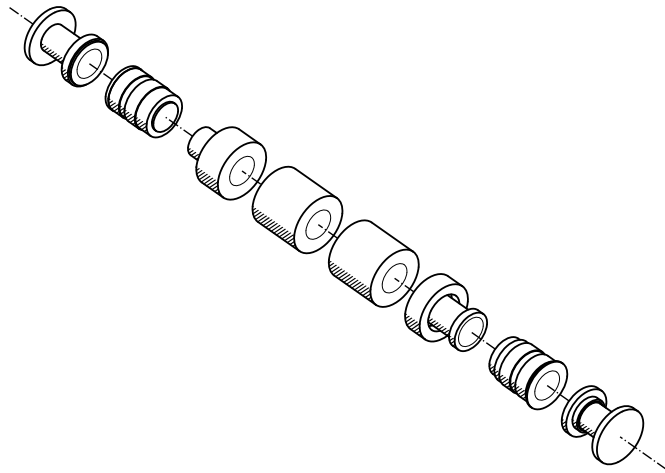
Figure 49: CAD geometry for the sCO₂ rotor divided into eight pieces

To obtain datapoints for flexural rigidity, a static structural simulation is performed where the rotor is subjected to z-moments of plus and minus 10^5 Nm at its ends, causing a uniform bending moment of this magnitude to appear throughout its length. The y-component of the resulting deflection is probed at 20 points along the rotor axis, and the 2nd x-derivative of deflection, y'', is estimated at all but the first and last points using the central difference method; the first value of y'' is simply approximated by the second, and the last by the last-but-one. The flexural rigidity at each point is calculated by dividing 10^5 Nm by y''. An expression for $EI(x)$ is finally arrived at by fitting a 17th degree polynomial to this data.
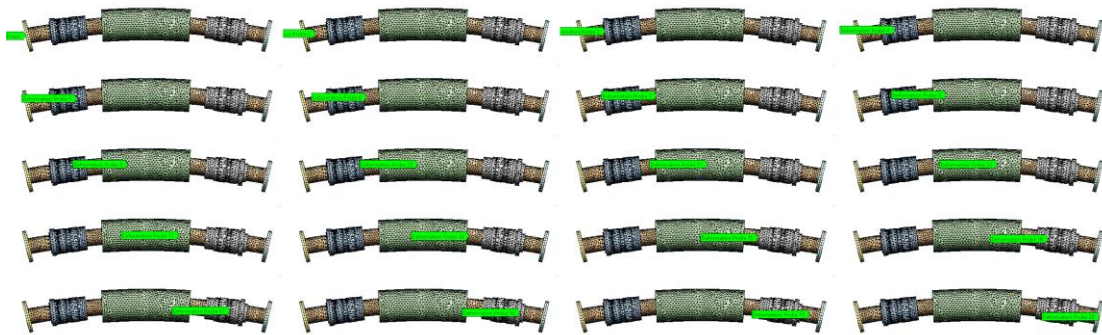

Figure 50: Static structural simulation with 20 deflection probes along the length of the rotor

Since the contribution of the laminated core to shear rigidity is particularly small, shear rigidity is estimated simply by calculating the radius of a circular steel beam that would show each calculated value of flexural rigidity, and then finding the expected

shear rigidity of such a beam. A 17th degree polynomial is fit to this data to serve as the expression for $KAG(x)$.

The polynomials obtained for $\rho A(x)$, $J_a(x)$, $EI(x)$, and $KAG(x)$ as described are shown plotted in Figure 51. Predictions of natural frequencies and a Campbell diagram obtained using these polynomials and twelve assumed mode shapes are compared in Section 5.6.3 with results from two commercial software packages: Ansys 2021 R1 and AxSTREAM RotorDynamics.
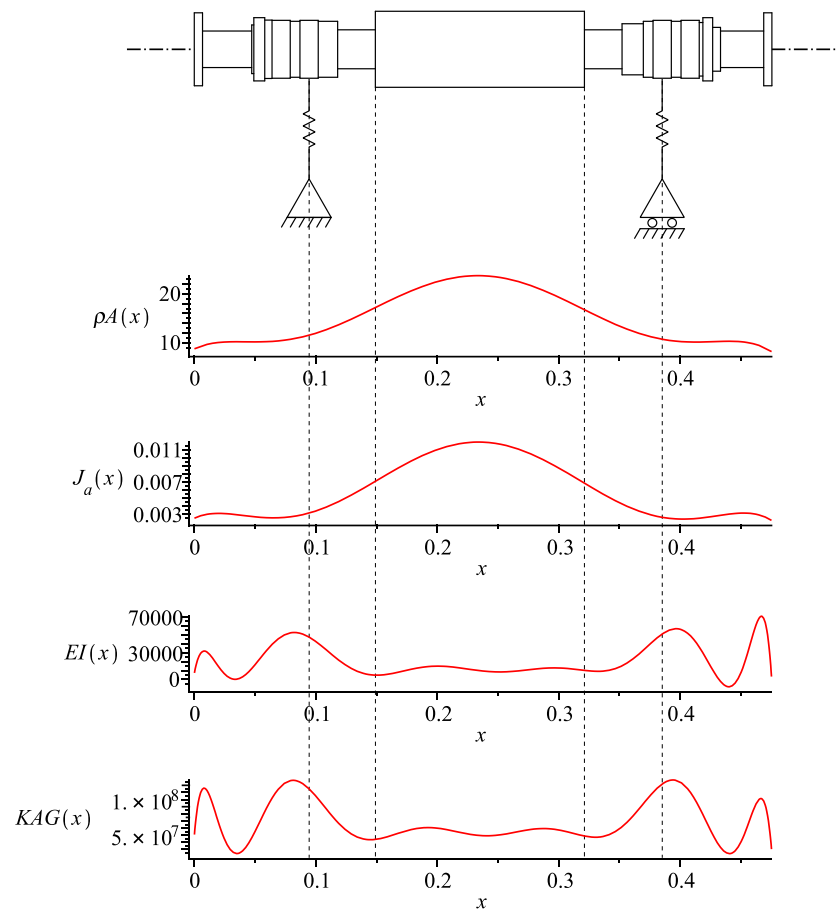
Figure 51: Polynomials fit to characteristics of sCO$_2$ rotor

5.6. Results and Discussion

Results and inferences from the two test cases described and from the modelling and analysis of the sCO$_2$ rotor now follow.

5.6.1. Results for the Tapered Hollow Rotor

The tapered hollow rotor is considered first on rigid bearings and then on compliant bearings of three different stiffnesses.

5.6.1.1. Tapered Hollow Rotor on Rigid Bearings

A Campbell diagram for the tapered hollow rotor on rigid bearings, obtained as described in Section 5.3, is shown in Figure 52. The Campbell diagram plotted by Ansys for the same geometry, with a mesh size of 1 cm (where refining the mesh from 2 cm to 1 cm had no significant effect on the output) is shown in Figure 53.
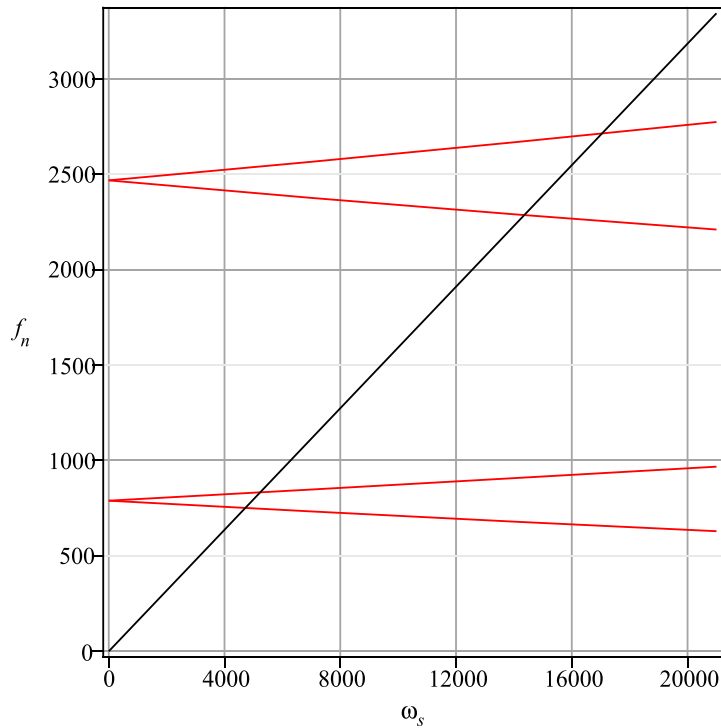
Figure 52: Campbell diagram for tapered hollow rotor on rigid bearings, from assumed modes formulation
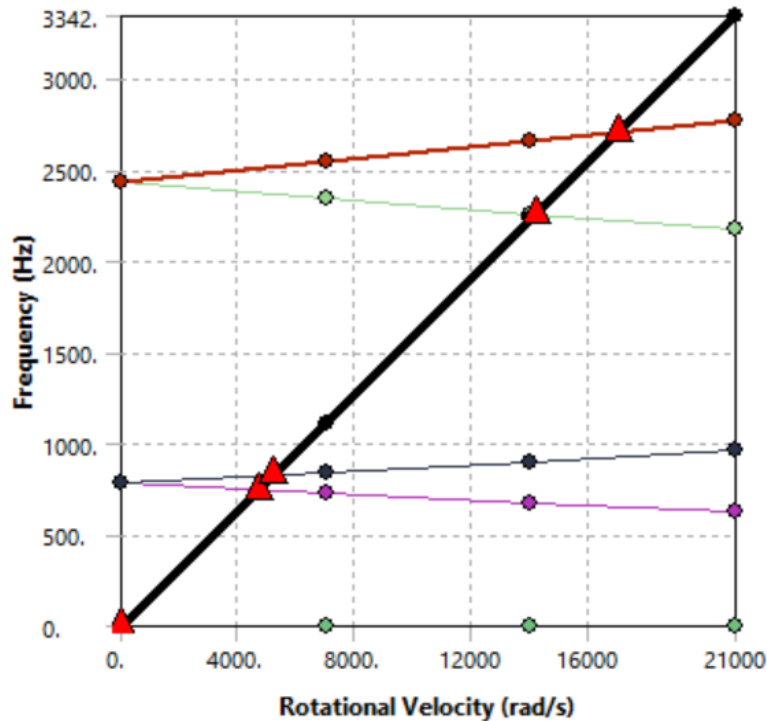
**Figure 53: Campbell diagram for tapered hollow rotor on rigid bearings, from Ansys 2021 R1**

Table 1 shows the first four natural frequencies of this rotor as predicted by the assumed modes method and by Ansys, at four different spin speeds. The agreement is good, with about 1% error.

Table 1: Natural frequencies (in Hertz) predicted for the tapered hollow rotor on rigid bearings

	ω_s (rad/s)	Mode 1	Mode 2	Mode 3	Mode 4
Using Assumed Modes	0	789	789	2467	2467
	7000	733	848	2375	2564
	14000	679	907	2289	2667
	21000	629	967	2209	2773
Ansys 2021 R1 Results	0	782	782	2438	2438
	7000	726	841	2344	2541
	14000	673	902	2258	2653
	21000	623	964	2179	2775

5.6.1.2. Tapered Hollow Rotor on Compliant Bearings

Table 2 shows natural frequency predictions for the tapered hollow rotor, at two different spin speeds and with three different bearing stiffnesses. Agreement with Ansys results is good, with less than 2% error.

Table 2: Natural frequencies (in Hertz) predicted for the tapered hollow rotor on bearings of varying stiffness at two spin speeds

Bearing Stiffness	Method	ω_s (rad/s)	Mode 1	Mode 2	Mode 3	Mode 4
10^8N/m	Assumed Modes	0	478	478	674	674
		21000	452	487	555	833
	Ansys 2021 R1	0	477	477	669	669
		21000	452	486	553	840
10^9N/m	Assumed Modes	0	776	776	1408	1408
		21000	618	945	1371	1461
	Ansys 2021 R1	0	770	770	1388	1388
		21000	615	946	1354	1448
10^{10}N/m	Assumed Modes	0	787	787	2355	2355
		21000	627	965	2130	2619
	Ansys 2021 R1	0	781	781	2318	2318
		21000	623	963	2101	2603

5.6.2. Results for the Multi-Stepped Rotor

Three Campbell diagrams for the multi-stepped rotor are shown in Figure 54, Figure 55, and Figure 56. The first is obtained through modelling the rotor using polynomials fit to calculated datapoints, the second using direct piecewise formulae, and the third from Ansys, with a mesh size of 5 mm. Table 3 shows the three corresponding sets of predictions of natural frequencies at four spin speeds. Agreement is reasonable but not excellent, with error up to 10%.

Discontinuity in the flexural and shear rigidities of a beam cause discontinuities in its slope and curvature when bent. The error observed here is presumed to be due to the inherently smooth polynomial assumed modes' inability to fully capture such discontinuities. The predictions are observed to move closer to the Ansys results as the number of assumed modes is increased. This suggests that the use of polynomial assumed mode shapes is best suited to rotors that have smoothly varying rigidity and inertia along their length or have relatively small discontinuities.

It can be seen that the slope of the lines in the Campbell diagram, i.e., the gyroscopic effect on natural frequencies, is captured fairly well.
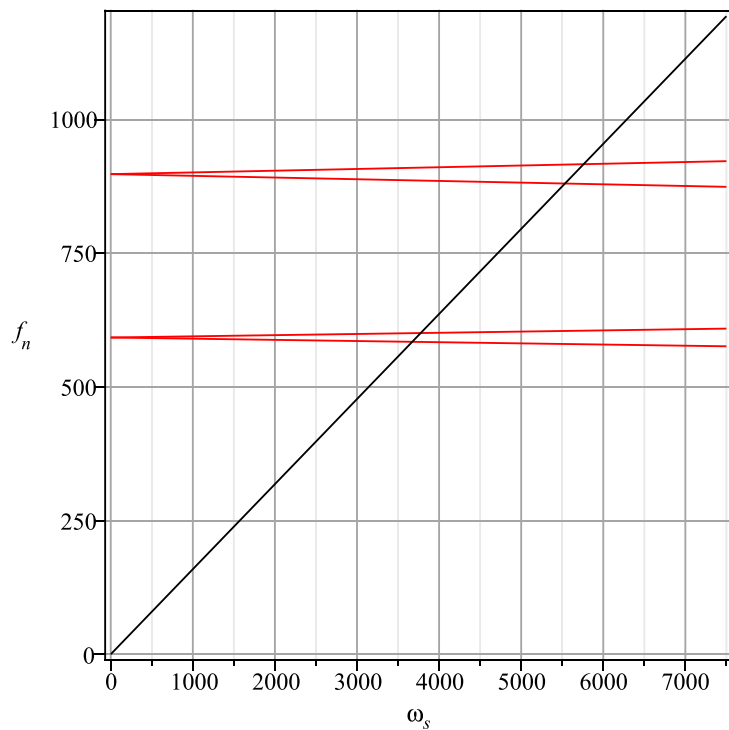
Figure 54: Campbell diagram for multi-stepped rotor modelled using polynomial fitting

Table 3: Natural frequencies (in Hertz) predicted for the multi-stepped rotor

|	ω_s (rad/s)	Mode 1	Mode 2	Mode 3	Mode 4
Using Polynomial Fitting	0	593	593	898	898
	2500	587	598	890	906
	5000	582	604	882	914
	7500	576	609	874	923
Using Piecewise Formulae	0	598	598	976	976
	2500	592	604	969	984
	5000	586	610	961	992
	7500	580	615	954	1000
Ansys 2021 R1 Results	0	542	542	917	917
	2500	536	548	909	924
	5000	530	554	902	932
	7500	525	560	895	940
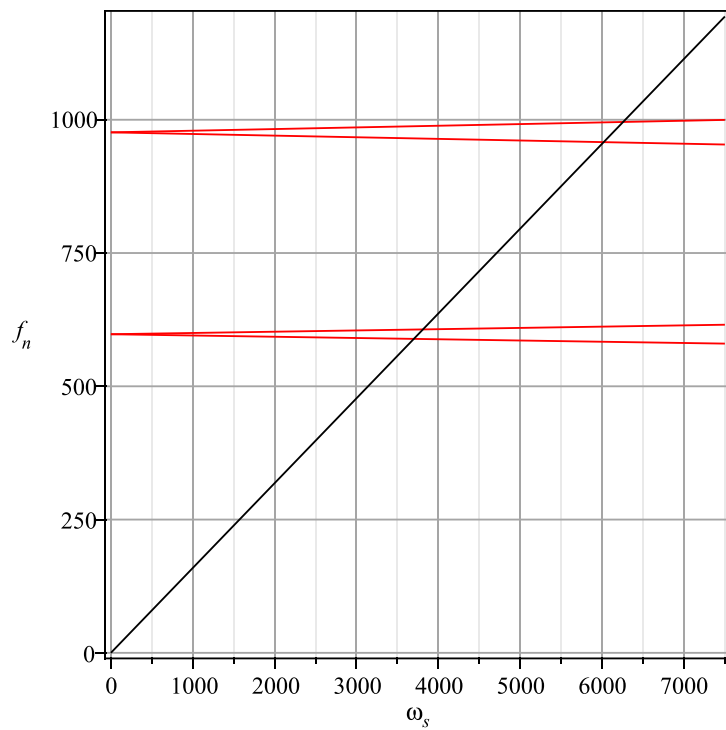
**Figure 55: Campbell diagram for multi-stepped rotor modelled using piecewise formulae**
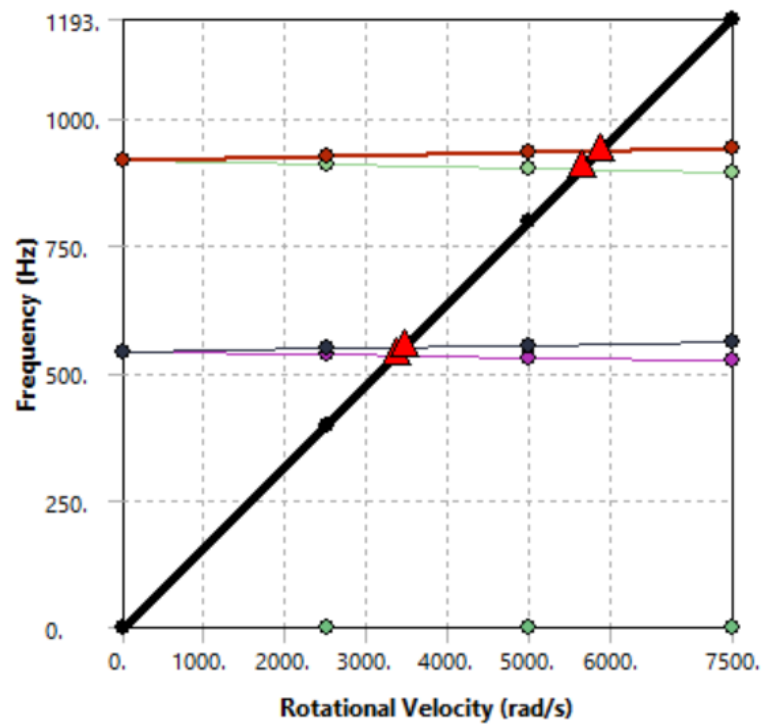
Figure 56: Campbell diagram for multi-stepped rotor from Ansys 2021 R1

82

5.6.3. Results for the Simplified sCO₂ Rotor

Figure 57 shows the Campbell diagram obtained for the simplified sCO_2 rotor using polynomials fit to data obtained as described in Section 5.5. Figure 58 shows the Campbell diagram plotted for this rotor by Ansys, with a mesh size of 5 mm. Figure 59 shows the Campbell diagram for equivalent geometry with the same assumed material properties and bearing stiffnesses, as plotted by AxSTREAM RotorDynamics. Natural frequency predictions at four evenly spaced spin speeds by Ansys, by AxSTREAM, and using the polynomial-fit model are shown in Table 4. Agreement of the results from the assumed modes formulation with both other sets of predictions is decent, with less than 3% error. The results from the assumed modes formulation match more closely with Ansys for the 1st and 2nd modes, and more closely with AxSTREAM for the 3rd and 4th modes.
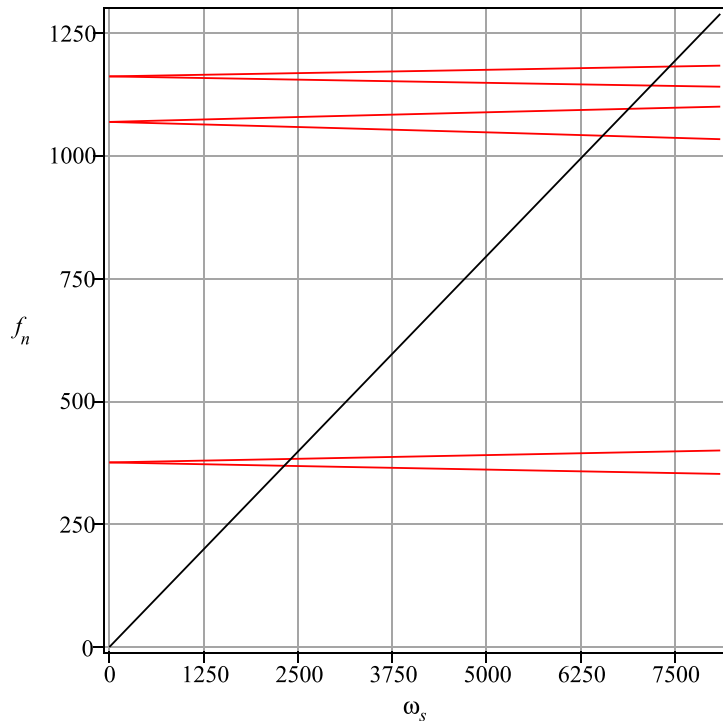
**Figure 57: Campbell diagram for the sCO₂ rotor modelled using polynomial fitting**
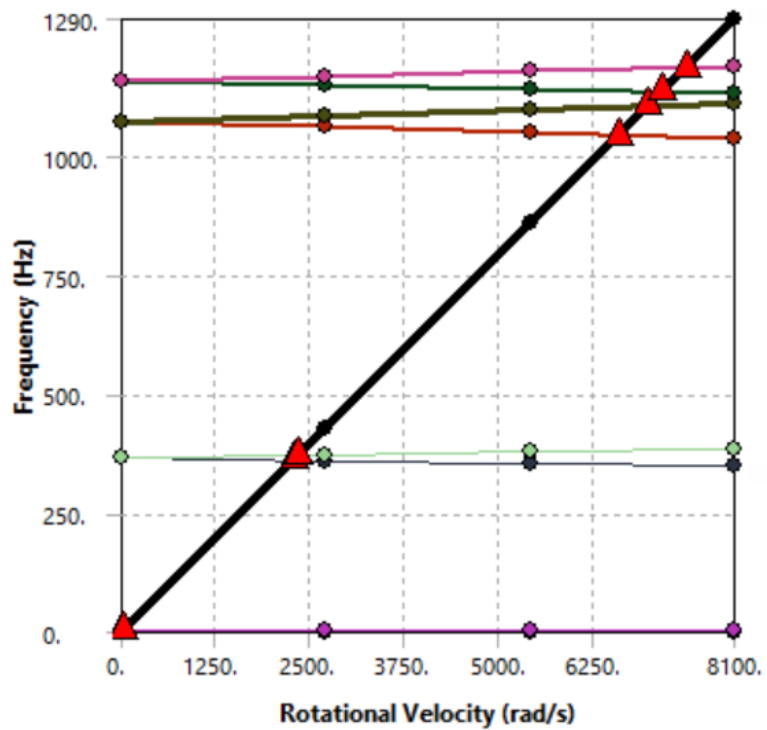
Figure 58: Campbell diagram for the sCO₂ rotor from Ansys 2021 R1
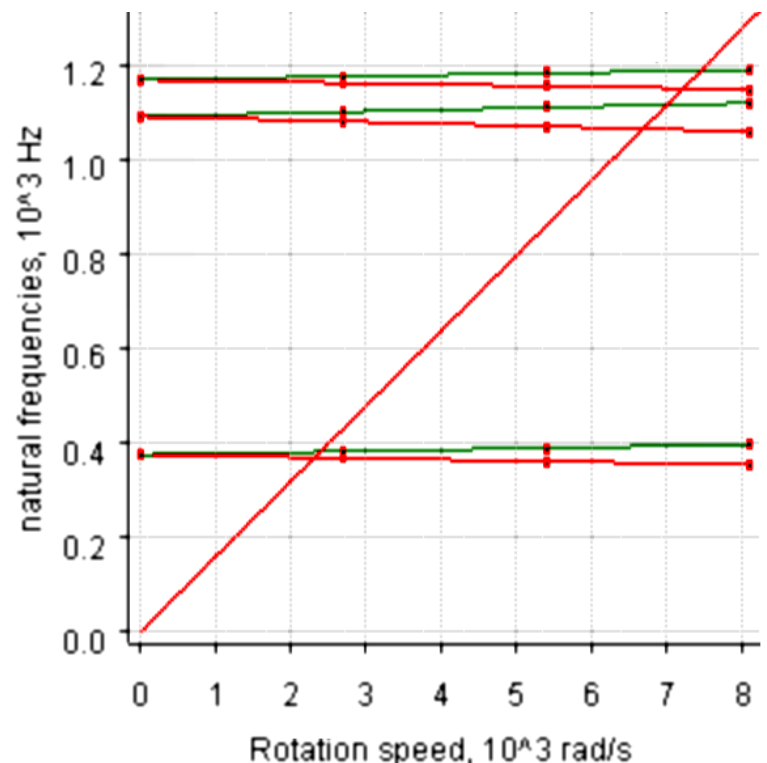

Figure 59: (Scaled to fit page) Campbell diagram for the sCO₂ rotor plotted by AxSTREAM

Table 4: Natural frequencies of the sCO$_2$ rotor (in Hertz) predicted by Ansys and by the polynomial-fit rotor model

	ω_s (rad/s)	Mode 1	Mode 2	Mode 3	Mode 4
Using Polynomial-Fit Rotor Model	0	376	376	1069	1069
	2700	368	384	1058	1080
	5400	360	392	1046	1090
	8100	353	400	1034	1100
Ansys 2021 R1 Results	0	367	367	1075	1075
	2700	361	374	1063	1088
	5400	355	380	1051	1100
	8100	349	387	1038	1112
AxSTREAM Results	0	375	375	1090	1090
	2700	368	382	1080	1100
	5400	362	390	1069	1109
	8100	355	397	1058	1118

6. CONCLUSIONS

This work has shown that a wide range of analytical models of varying levels of complexity can serve both as useful tools to predict rotor whirl and as effective aids to help understand it. In general terms, it is clear from the results seen here that the minute details of rotor geometry are often not particularly important in the prediction of whirling behaviour. A low-resolution rotor model that captures the variation of a rotor's essential characteristics along its length can greatly improve the transparency, and thereby the explanatory power, of analytical calculations, with minor sacrifice of accuracy of results.

More specifically, this work shows firstly that a Lagrangian formulation with polynomial assumed modes can be an effective approach to predicting whirl in rotors whose rigidity and inertia vary smoothly or with small discontinuities along their length, and secondly that, when used with such a formulation, curves fit to rigidity and inertia at points along the axis can serve as a reasonable rotor model.

Other conclusions that may be drawn from this work include that the perceived effect of Coriolis terms of a rotor depend entirely on the choice of reference frame, that gyroscopic terms need not be added separately in rotor formulations when a consistent reference frame is used, and that the use of polynomial assumed modes is best suited to rotors that have smoothly varying properties along their length or only have small discontinuities.

7. SCOPE FOR FUTURE WORK

One of the drawbacks identified of the method this thesis presents is that polynomial assumed modes are not ideally suited to stepped shafts, or otherwise to rotors with large discontinuities in geometry or material properties along their length. As such, it may be speculated that significant improvements could be made to the versatility of this method through study of alternative bases of assumed mode shapes.

The model presented in this thesis contains a rudimentary accounting of bearing compliance through the inclusion of a simple radial spring constant at the support locations. In real rotor systems, the axial stiffnesses of bearings are sometimes of significant importance. Such effects may be modelled in future work. Moreover, this thesis only studied unloaded rotors, so extension of the model to capture axial and/or transverse loading might prove valuable. Work may also be done on the inclusion of damping effects, which are unusually varied and complex in rotor systems.

8. REFERENCES

[1] F. C. Nelson, Rotor Dynamics without Equations. International Journal of COMADEM, 2007

[2] Allison, T., Wilkes, J., Brun, K., & Moore, J., Turbomachinery overview for supercritical CO2 power cycles. Proceedings of the 46th Turbomachinery Symposium. Turbomachinery Laboratory, Texas A&M Engineering Experiment Station, 2017

[3] S. H. Choi, C. Pierre, A. G. Ulsoy, Consistent Modelling of Rotating Timoshenko Shafts Subject to Axial Loads. J. Vib. Acoust., 1992

[4] Han, R. P., and Zu, J. W. Z., Analytical dynamics of a spinning Timoshenko beam subjected to a moving load. Journal of the Franklin Institute, 1993

[5] P.A.A. Laura, S. La Malfa, L.Ercoli, V.H. Cortínez, Whirling of flexible shafts with intermediate supports. Applied Acoustics Volume 21, 1987

[6] Shiau, T. N., and Hwang, J. L., A New Approach to the Dynamic Characteristic of Undamped Rotor-Bearing Systems. ASME. J. Vib., Acoust., Stress, and Reliab., 1989

[7] H. Fang, B. Yang, Modelling, synthesis and dynamic analysis of complex flexible rotor systems. Journal of Sound and Vibration, 1998

[8] R. Norouzi, M. Rafeeyan, H. Dalayeli, Vibration analysis of a multi-disk, bearing and mass unbalance rotor using assumed modes method. International Journal of Advanced Design and Manufacturing Technology, 2015

[9] Afshari, H., Irani Rahaghi, Whirling analysis of multi-span multi-stepped rotating shafts, J Braz. Soc. Mech. Sci. Eng., 2018

[10] Pradeep Mahadevan, C.S. Jog, Anindya Chatterjee, Modal projections for synchronous rotor whirl, Proc. R. Soc. A, 2008

[11] R. Whalley, A. Abdul-Ameer, Whirling prediction with geometrical shaft profiling. Applied Mathematical Modelling, 2009

[12] Yixin Huang, Tianshu Wang, Yang Zhao, Pingping Wang, Effect of axially functionally graded material on whirling frequencies and critical speeds of a spinning Timoshenko beam. Composite Structures, 2018

[13] Abdelhak Elhannani, Kaddour Refassi, Abbes Elmeiche, and Mohamed Bouamama, Vibration analysis of functionally graded tapered rotor shaft system. Mechanics and Mechanical Engineering, 2019

[14] S.D. Garvey, The vibrational behaviour of laminated components in electrical machines. Fourth International Conference on Electrical Machines and Drives, 1989

[15] SD Garvey, JET Penny, MI Friswell, AW Lees, The stiffening effect of laminated rotor cores on flexible-rotor electrical machines. Strain, 2004

[16] Hutchinson, J. R., Shear Coefficients for Timoshenko Beam Theory. ASME. J. Appl. Mech, 2001